The 2008 and 2012 Moosiyan Earthquake Sequences: rare insights into the role of strike slip and thrust faulting within the Simply Folded Belt (Iran).

Stuart E.J. Nippress, Ross Heyburn, and R.J. Walters

Address for correspondence

Dr. S.E.J. Nippress

AWE Blacknest

Brimpton

Reading

RG7 4RS

United Kingdom

stuart@blacknest.gov.uk

ABSTRACT

The Zagros mountain belt has an unusually large discrepancy between seismic and geodetic strain rates, implying very large aseismic release of strain. However, the spatial and depth relationship between seismic and aseismic deformation is poorly understood and controversial, with important implications both for understanding the role of aseismic deformation in regions of continental convergence and characterising seismic hazard for large urban populations in this region. Two recent earthquake sequences in 2008 and 2012 provide us with an ideal opportunity to use geodetic and seismological data to address this topic, not only for thrust faulting, but also for rarer strike-slip faulting in the Zagros. These aftershock sequences occurred on the south-east border between Iran and Iraq. We use Interferometric Synthetic Aperture Radar (InSAR) to obtain a mechanism for the 2008 mainshock, and observed significant aseismic slip accompanying the earthquake. This aseismic slip occurred along strike from the seismic asperity and approximately doubled the seismic moment release, demonstrating that aseismic slip plays an important role for strike-slip as well as thrust faulting in the Zagros. Depths are calculated by inverting surface wave amplitude spectra and depth phase observations demonstrating that all events occur at depths less than 12 km, supporting the view that seismicity predominately occurs in the sedimentary cover in the Zagros. Using both the calculated depths and InSAR location we relocate the aftershocks to reveal two distinct clusters, with the 2012 cluster occurring in the vicinity of the Zagros Foredeep Fault, challenging the traditional view that this region is aseismic.

INTRODUCTION

In 2008 and 2012, three moderately-sized earthquakes and their aftershock sequences occurred in south-western Iran on the Iran-Iraq border (Figure 1). The first and largest (M_w 5.8) of these earthquakes struck, early in the morning on the 27^{th} August 2008. There then followed a period of nearly four years before the second earthquake struck again early in the morning on the 28^{th} February 2012 (M_w 5.0). The third moderately-sized earthquake (M_w 5.2) occurred on the 20^{th} April 2012 at 05:51 local time. Although the magnitudes of these earthquakes and their aftershock sequences are quite small, what distinguishes them compared to other seismicity in the region is that

their initial locations placed these events within the Simple Folded Belt (SFB) in the vicinity of the Zagros Foredeep Fault (ZFF), a region which is thought to be largely aseismic (Nissen et al., 2011). Furthermore, the calculated focal mechanisms for the 27^{th} of August 2008 earthquake describe a strike-slip motion that is uncommonly observed in the convergent environment of the SFB.

There has been significant recent debate on the depth of seismicity in the Zagros and its relationship with the local stratigraphy (e.g. Nissen et al., 2011; Barnhart and Lohman, 2013; Nissen et al., 2014). Most discussion has focused on whether earthquakes mainly occur in the crystalline basement or the overlying sedimentary cover, and how the interleaving salt layer may limit earthquake size by inhibiting rupture propagation between the cover and basement (e.g. Nissen et al., 2011). A related debate is concerned with the role of aseismic deformation in this region. It has long been known that the summed seismic moment release across the Zagros only accounts for a small amount of the geodetically measured shortening (Jackson and McKenzie, 1988; Masson et al., 2005). Current debate is focused on whether earthquakes in the Zagros are commonly related to aseismic triggered events of comparable magnitude, and if those aseismic events occur in the same or a different stratigraphic layer as the triggering earthquake (Barnhart and Lohman, 2013; Nissen et al., 2014; Elliott et al., 2015). Much of this discussion has focused on thrust faulting, as it is more common than strike-slip faulting in the SFB, but the 27^{th} of August 2008 earthquake provides a rare opportunity to comment on how strike-slip faulting in the Zagros relates to these ideas.

In this paper we use both seismological and InSAR data to present a combined seismotectonic analysis of the 2008 and 2012 sequences close to the Iran-Iraq border. We use seismological data to determine the source parameters and the location of the causative faults, complemented by InSAR data for the largest M_w 5.8 strike-slip event on the 27^{th} August 2008. We determine the source parameters of the three main shocks, as well as some aftershocks through surface wave amplitude spectra modeling. The location and orientation of the 27^{th} August 2008 fault source is constrained through modelling of Interferometric Synthetic Aperture Radar (InSAR) data. Improved epicentral locations for 89 earthquakes are calculated using a joint location method and provide the locations of the aftershocks and their depth range. The seismological and InSAR constraints are then used to address the wider subject of active deformation of the SFB, in particular the depth extent of seismicity and the role of aseismic deformation.

TECTONIC AND GEOLOGICAL SETTING

The tectonics in south-western Iran is dominated by the continual northward motion of Arabia converging with the Eurasian plate. Approximately half of the shortening ($\sim 25 mm yr^{-1}$) is taken up by the Zagros mountains (Vernant et al., 2004), with the remainder accommodated in the Alborz and Kopeh Dagh mountains in northern Iran. The Zagros mountains run continuously for 2000 km between eastern Turkey and SE Iran and can be subdivided into the High Zagros and the Simply Folded Belt (SFB) based on topography, stratigraphy and seismicity (e.g. Berberian, 1995). The SFB can be further subdivided based on elevation, with the low-lying Dezful Embayment (the location of this study, Figure 1) located between two regions of high relief (the Lurestan Arc to the north-west and the Fars Arc to the south-east). The Dezful Embayment appears to be a discrete structural unit bounded by the Mountain Front Fault (MFF) to the north-east, the Zagros Foredeep Fault (ZFF) to the south-west, the right-lateral Kazerun strike-slip fault (trending NNW-SSE through the Zagros at around longitudes $51 - 52^{\circ} E$) to the east and the Balarud line (a strike-slip fault or basement step) to the north (Allen and Talebian, 2011).

The stratigraphy of the Zagros records the evolution from the passive margin of the Arabian plate to the foreland basin of the Arabian-Eurasian collision (Allen and Talebian, 2011). The Precambrian basement is not exposed at the surface but thought to be at a depth of 13 km (based on well and field data and a review of the literature (Casciello et al., 2009)) or 12 km (from cross-sections based on the geological map from the National Iranian Oil Company (Motagh et al., 2015)) and 12 km depth (from long wavelength aeromagnetic studies (Morris, 1977)). These estimates are not from direct observations and are based on balancing geological cross-sections and the non-unique interpretation of magnetic anomalies. Therefore, the depth of basement of ~13 km will have some error associated with it and could very well be deeper. Above the basement lies the Hormuz series of thick evaporites of Precambrian/Cambrian age. However, due to a lack of salt diapirs reaching the surface in the Dezful Embayment, the presence of Hormuz salt in this area is debated (e.g. Nissen et al., 2011). The 'competent group' (O'Brien, 1957), a single structural group that is dominated by carbonates and clastics, overlies the basement and a mobile evaporate layer (the Gachsaran formation) is found in the lower-Miocene (the 'upper mobile group' (O'Brien, 1957)) creating a weak mechanical layer

above this 'competent group'. The shallowest mid-Miocene and younger rocks consist of sandstones and shales that form the 'incompetent group' (O'Brien, 1957), and the thickness of this group varies significantly across the fold-thrust belt.

The faulting in the SFB and particularly the Dezful Embayment is dominated by thrust faults. The MFF, ZFF and Dezful Embayment Fault (DEF) are termed 'master blind thrusts' and are inferred by Berberian (1995) based on mapped steps in exposed stratigraphic levels rather than faults that are actually exposed at the surface. The MFF in the Dezful Embayment marks the limit of the Eocene-Oligocene Asmari limestone outcrops with vertical displacements along this thrust of $\sim$6 km (Berberian, 1995). The ZFF, principally a reverse-slip system, runs roughly parallel to the MFF with a throw of 3 km in the Dezful Embayment (Berberian, 1995). The DEF is a shorter blind thrust fault that displays a vertical displacement of 1-3 km based on geological evidence (Berberian, 1995). The Balarud line trends east-west which is oblique to the predominant trend of the SFB. The displaced folds observed around the Balarud line has been used to suggest this feature is either a left-lateral strike-slip fault (Berberian, 1995) or a step in the basement (deeper in the Embayment compared to the North), rather than a steeply dipping fault (Allen and Talebian, 2011).

The seismicity of the high Zagros is dominated by strike-slip events with only a small number of thrust earthquakes (Figure 1 and Talebian and Jackson (2004)) and is generally linked to the Main Recent Fault (MRF) and parts of the High Zagros Fault (HZF). Generally, the earthquakes that occur along the MRF have larger magnitudes than those in the SFB (Berberian, 1995). The SFB has significantly more seismicity and is dominated by blind thrust faulting (Figure 1 and Nissen et al. (2011)), although strike-slip faulting does play an important role. The thrust events in the SFB generally strike parallel to the trend of the range with steep dips ($30^\circ - 60^\circ$), inherited from older normal faults in the stretched Arabian margin (e.g. Jackson, 1980). Centroid depths for these thrust earthquakes are generally between 4 - 10 km depth (Nissen et al., 2011), suggesting they are located within the sedimentary cover. Another notable characteristic of the SFB is the predominance of moderate-sized earthquakes (M_w 5-6) and the complete absence of any events with $M_w > 7$ (Nissen et al., 2011). Within the area of the Dezful Embayment the seismicity is clustered along the northern margin in close proximity to the MFF and DEF blind thrust faults. These events display thrust mechanisms with moderate magnitudes (M_w <6.6). Apart from the earthquake sequences in 2008

and 2012, seismicity is absent from just south-east of Ahvaz for ∼400 km along the ZFF. The only strike-slip earthquake in the last 25 years recorded teleseismically along the ZFF in the Dezful Embayment is the 27^{th} of August 2008 event.

THE 2008 AND 2012 EARTHQUAKE SEQUENCES

On the 27^{th} of August 2008 (21:52 UTC, 01:22 local time) a M_w 5.8 earthquake occurred in a remote desert region of the Zagros Simply Folded Belt in south-west Iran, close to the Iran-Iraq border (Figure 1). The rupture occurred ∼20 km south of the city of Moosiyan, in the Ilam Province. The initial epicentral locations placed this event at $32.308°N$ $47.350°E$ and 10 km depth (USGS, PDE) and $32.23°N$ $47.36°E$ at a depth of 12.5 km (Global CMT). Although no injuries or damage were reported for this earthquake in the local region it was felt with an intensity of IV (instrument intensity USGS) in the town of As Salimiyah, Kuwait, a distance of ∼330 km away. In the following three months 10 aftershocks were recorded teleseismically and 30 by the in-country Iranian networks.

In the following two years 9 earthquakes were recorded teleseismically in the vicinity of the 2008 earthquake but only three had magnitudes of M_w >4.1. At the end of February 2012 seismic activity in this region increased and migrated ∼46 km north-westwards of the 2008 earthquake (Figure 1). On the 28^{th} February 2012 at 23:18 UTC (02:48 local time) a M_w 5.0 earthquake occurred. The initial epicentral locations placed this event at $32.503°N$ $46.913°E$ and 10 km depth (USGS, PDE) and $32.58°N$ $46.81°E$ at a depth of 12.5 km (Global CMT). Fortunately, although felt in the local region, this earthquake also caused no damage to buildings or injuries to local people. Following this event 10 teleseismically recorded earthquakes were observed between 28^{th} February 2012 and 19^{th} April 2012.

Then on the 20^{th} April 2012 at 01:21 UTC (05:51 local time) a M_w 5.2 earthquake occurred ∼38 km to the west of the 2008 earthquake and ∼10 km east of the 28^{th} February 2012 earthquake (Figure 1). The initial epicentral locations placed this event at $32.511°N$ $47.023°E$ and 10 km depth (USGS, PDE) and $32.53°N$ $46.83°E$ at a depth of 12.0 km (Global CMT). This earthquake was strongly felt ∼31 km away in the town of Dehloran, Iran. In the following 3 months 30 aftershocks were recorded teleseismically and 50 by the Iranian networks (of which 13 and 21 respectively occurred on the same day as the mainshock).

FAULT GEOMETRY AND SLIP DISTRIBUTION DETERMINED USING INSAR

We used SAR interferometry to measure ground displacements due to the 27^{th} of August 2008 earthquake, and used elastic dislocation models to obtain source parameters for the earthquake, including a precise location that is independent of seismological estimates. Repeated radar acquisitions covering the epicentral region are available for two ENVISAT tracks with ascending and descending viewing geometries. We processed a single pair of SAR acquisitions for ascending track 42, spanning dates 25^{th} of January 2007 to 9^{th} of April 2009, and two pairs for descending track 235, spanning dates 23^{rd} of February 2006 to 22^{nd} of July 2010 and 15^{th} of November 2007 to 4^{th} of March 2010. We processed the InSAR data from raw data products using the JPL/Caltech ROI_PAC software (Rosen et al., 2004). The interferograms were corrected for differences in satellite position using DORIS satellite orbits from the European Space Agency (ESA), and topographic signals were removed using a 3-arc-second ($\sim$90 m) resolution Shuttle Radar Topography Mission (SRTM) Digital Elevation Model (DEM) (Farr et al., 2007). Interferograms were filtered using a power spectrum filter (Goldstein and Werner, 1998) and unwrapped using the branch cut method.

The ascending and descending interferograms show a simple deformation signal represented by a single lobe with two local maxima (Figure 2). We have confidence that this 'double maxima' signal is real and not due to atmospheric contamination of the InSAR data as it is present in three independent datasets; the single ascending and both descending interferograms (Figure S1, available in the electronic supplement to this article). The deformation signal is smaller in the two descending interferograms and approaches the noise level in the data (1σ of $\sim$4 mm in the satellite line-of-sight). Therefore, to increase the signal-to-noise ratio of the data we stacked the two images; taking the average displacement for each pixel that is coherent in the both descending interferograms. This 'stacked interferogram' was used at descending data input in the following processing steps.

The interferograms were downsampled using a quadtree algorithm (e.g. Jónsson et al., 2002), reducing the number of data points for each interferogram to $\sim$750 (Figure S2, available in the electronic supplement to this article). The subsampled data sets were jointly inverted for uniform slip on a rectangular fault plane in an elastic half-space (Okada, 1985), using a Powell optimization algorithm with multiple Monte Carlo restarts to find the best-fitting combination of fault parameters

(e.g. Wright et al., 2003). We use values of $\lambda = \mu = 2.06 \times 10^{10}$ Pa for elastic Lamé parameters, which are chosen to be consistent with the shallow crustal velocity structure calculated from locally-recorded aftershock arrival times by Nissen et al. (2011) and used in that study for a body-waveform inversion of this earthquake (Table 1). The resulting solution fits the data well and has an RMS misfit to both data sets of 4 mm. This is similar to the 1σ estimates of noise in the data and much smaller than peak displacement in each dataset ($\sim$30 mm for the ascending interferogram and $\sim$20 mm for the descending interferogram). The predicted ground displacements have a good visual fit to the data and small residuals (see Supplementary Figure S3, available in the electronic supplement to this article). The best fitting solution (Figure S3, available in the electronic supplement to this article) describes a right-lateral fault with a small thrust component (rake=158°), striking NW-SE and steeply dipping to the SW (Table 1). The model fault has larger length and smaller width ($\sim$40 km and $\sim$3 km respectively) than is known to be common for a M_w 5.8 earthquake from earthquake scaling relations (expected length and width $\sim$9 km and $\sim$7 km respectively, Wells and Coppersmith (1994)). Whilst the 40 km fault length is a robust feature and is required by both the ascending and descending InSAR data, it is clear from the uncertainty analysis (Figure S4, available in the electronic supplement to this article) that fault width trades off against the magnitude of slip. However, all other parameters are unaffected by re-running the inversion with the slip fixed to a more realistic value (25 cm), so this trade-off appears not to affect the fault geometry. The InSAR data clearly resolve the nodal plane ambiguity inherent in the seismological focal mechanisms; the elongation of the deformation lobes requires that the fault strikes SE. The fault, strike, dip and rake are similar to the seismological estimates, but the geodetic moment is at least twice as large as the seismic moment (Table 1). The seismological estimates of strike, dip and rake do not fall within the bounds estimated from the InSAR uncertainty analysis. However the uncertainties included in Table 1 only reflect the impact of aleatoric uncertainty on the model, and not the epistemic uncertainty of the assumption of a single fault plane. The geodetic signal is too small to warrant the extra complexity of multiple fault planes, but the discrepancy between the InSAR and seismological strike, dip and rake could be because the InSAR also includes additional complexity from the postseismic deformation, which could have a slightly different mechanism or geometry.

We also performed a distributed slip inversion by fixing the fault geometry to that obtained from

the uniform slip model, extending the fault-plane in both length and width, and discretizing the plane into ∼2 km by 2 km rectangular patches. We then solved for slip on this array of patches, regularizing the inversion with Laplacian smoothing (e.g. Wright et al., 2003; Funning et al., 2005). The resulting slip distribution is shown in Figure 2g. Although the distributed slip model provides only a slightly better fit to the data than the uniform model (RMS misfit of 3.99 mm vs. 4.14 mm), the model does not collapse to a line source with narrow fault width and high slip and so likely represents a more realistic pattern of slip. As such, this is our preferred model and is shown in Figure 2, although the uniform model is also shown for comparison in Figure S3 (available in the electronic supplement to this article). The slip distribution clearly features two discrete asperities, both centered at around 10 km depth and both around 15-20 km in length. These two asperities are robust features of this inversion; they are required to qualitatively explain the double maxima of displacement seen in both ascending and descending interferograms (Figures 2, Figure S1, available in the electronic supplement to this article), are resolved above the estimated 2-sigma uncertainties on the slip distribution (Figure 2g), and are independent of the strength of spatial smoothing applied during the inversion (Figure S5, available in the electronic supplement to this article). In addition, checkerboard resolution tests show that at 10 km depth, slip patches of 8-10 km width or greater are easily resolved (Figure S6, available in the electronic supplement to this article). Both uniform and distributed slip models feature a model fault that has significantly higher length than expected for a M_w 5.8 earthquake (∼9 km, Wells and Coppersmith (1994)), and a geodetic M_w of ∼6, corresponding to at least double the seismological estimates of moment release.

EVENT DEPTH DISTRIBUTION AND FOCAL MECHANISM ANALYSIS

Teleseismic Body Waves Observations

For earthquakes located in regions where there are no dense local networks of seismometers, accurate estimates of earthquake source depths can be obtained by identifying the teleseismic depth phases *pP* and *sP*, or using observations of surface wave amplitude spectra recorded at regional and teleseismic distances. Identifying the depth phases *pP* and *sP* on *P* seismograms recorded at long range is one of the most reliable ways of estimating the source depths of earthquakes (Stein and Wiens, 1986). For a given wave-speed structure for the source region, the difference in arrival time between *P* and

the depth phases can be used to estimate depth. Ideally the *P* seismograms should have a good signal-to-noise ratio (SNR), with *P*, *pP*, and *sP* being the dominant phases on the seismogram. However, confident identification of depth phases and hence depth estimation is sometimes difficult, as teleseismic *P* seismograms can be complex with no dominant phases in the time window after *P*.

For the events listed in Table 2 all seismograms recording teleseismic *P* in the Reviewed Event Bulletin (REB) have been reviewed by an analyst and an attempt has been made to identify the depth phase *pP*. For events where two or more *pP*s with good SNRs can be identified, the *pP*-*P* times are converted to a source depth using the IASPEI91 travel-time tables. Figure 3 shows selected short-period teleseismic *P*-wave seismograms recorded for the 27^{th} August 2008 M_w 5.8 earthquake. The seismograms are bandpass filtered with the passband which produced the largest SNR for direct *P*. All seismograms in Figure 3 display a clear arrival approximately 3.5 seconds after direct *P*, and this arrival is interpreted as the depth phase *pP*. A *pP*-*P* of around 3.5 seconds corresponds to a depth of approximately 11 km if the IASPEI 91 travel-time tables are used. For 32 of the events listed in Table 2, depths could be estimated in this way. One of the disadvantages of estimating the earthquake source depth in this way is that it is possible that the phase identified as *pP* is in fact *sP* and hence the earthquake depth is overestimated. In the following section source depths estimated using surface wave data for 6 of these 32 events are found to be consistent with the picked depth phase being *pP*. Section 6.2 also shows that the source mechanisms of the earthquakes analysed in this study are predominantly thrust faults. The *T* axis for thrust faults is close to the vertical hence *P* and *pP* will likely be the dominant phases on short-period seismograms recorded at teleseismic distance stations. If for any of the earthquakes analysed the phase *pP* has been misidentified as *sP* then that would reduce the estimated source depth. For example, *pP*-*P* times at teleseismic distances for a source depth of 11 km are approximately equivalent to *sP*-*P* times for a source depth of 8 km.

One of the principle causes of uncertainty in source depths estimated by depth phase identification is errors in the wave-speed models used to calculate the travel-times of the depth phases relative to *P*. Uncertainty in a depth estimate as a result of model error is approximately linearly related to the mean seismic wavespeed of the above-source structure. Therefore if model errors of 15% are expected, then the estimated depth should be within $\pm 15\%$ of the true source depth. In the

top 20 km of the crust the IASPEI 91 model has a P wave-speed (V_P) of 5.8 km s^{-1}. Previous studies of seismicity in the Zagros mountains have used various different values for the upper crust V_P. For example, Talebian and Jackson (2004) assumed an average V_P of 6.0-6.5 km s^{-1} where as more recent studies such as the one by Nissen et al. (2011) use a V_P of 5.0-5.6 km s^{-1} calculated by inverting locally recorded earthquake arrival times. The V_P of 5.8 km s^{-1} used here is approximately midway between these ranges for V_P and is therefore reasonable provided a 15% error in the V_P and hence the estimated source depths is allowed for.

Regional Surface Wave Modelling

Seismic source depths can also be estimated using observed surface wave amplitude spectra. Tsai and Aki (1970) demonstrated that the shapes of 50-10 s Rayleigh wave amplitude spectra are sensitive to changes in the depths of earthquakes. For example, frequency-dependent spectral nulls which can provide a tight constraint on source depth are sometimes seen in the observed Rayleigh wave amplitude spectra, and as source depth increases Rayleigh and Love wave spectral amplitudes drop appreciably (Patton, 1998). Building on the work of Tsai and Aki (1970) and Patton (1998), Fox et al. (2012) developed a method of estimating source depth, mechanism and scalar moment by modelling intermediate period (100-15 s) fundamental-mode Rayleigh and Love wave amplitude spectra. Many of the earthquakes analyzed in this study are too small to produce intermediate period surface waves which can be recorded at regional distances, but for 10 of the earthquakes we have been able to use the method of Fox et al. (2012) to estimate the source depth and mechanism, and for one further earthquake we have been able to estimate the source mechanism only.

To isolate the fundamental-mode Rayleigh and Love waves, phase-matched filtering (Herrin and Goforth, 1977) using phase velocity estimates from the 3-D CUB Earth model (Shapiro and Ritwoller, 2002) is applied to remove dispersion from the recorded waveforms. A 300 s Hann window is then applied to the observed surface waves to remove unwanted signals and noise. Following Fox et al. (2012), synthetic Rayleigh (vertical component only) and Love wave seismograms are generated. This is done by calculating the wave excitation in the local Earth structure at the source, making amplitude and path corrections due to propagation through the laterally heterogeneous 3-D CUB Earth model, and finally calculating the displacement dependent on the local Earth structure at the

receiver. For the earthquakes analysed here, synthetic seismograms are computed for source depths between 1 and 40 km at intervals of 2 km, and for all orientations of the double-couple source using steps of 5° for strike, dip and rake (co-ordinate system of Aki and Richards, 1980). Scalar moments are obtained for each focal mechanism and depth by scaling the unit synthetic amplitude spectra to the observed data. Computed synthetic surface wave amplitude spectra are then compared with the observed amplitude spectra (100-15 s period) using a least squares measure of misfit, m, which is defined as follows,

$$m = \frac{\sum_{j=1}^{T}\sum_{i=1}^{N}(\log d_{ij} - \log s_{ij})^2 \Psi_{ij}^2}{\sum_{j=1}^{T}\sum_{i=1}^{N}(\log d_{ij})^2 \Psi_{ij}^2}, \quad (1)$$

where T is the total number of traces, N is the number of discrete frequencies, d_{ij} and s_{ij} are the amplitudes of the data and synthetic amplitude spectra at the jth frequency on the ith trace, and Ψ_{ij} is the combination of applied weights. Ψ_{ij} consists of an azimuthal weight (defined as the inverse of the number of stations within a 10° azimuth range of the source), and a frequency-dependent weight ($\frac{1}{\omega}$) to apply greater weight to the longer-period end of the amplitude spectra.

For ten of the earthquakes large enough to generate intermediate period surface waves which can be recorded at regional distances, the depth could be well-constrained using the method outlined above. For example, Figure 4 displays a misfit-depth profile showing lower-hemisphere stereographic projections of the best-fitting focal mechanisms at each depth for the 3^{rd} September 2008 earthquake. Figure 4 shows that the misfit has a clear minimum at a depth of 9 km for a pure reverse fault with a mechanism of $\phi_s = 310°, \delta = 40°$ and $\lambda = 95°$. Figure 5 compares observed and synthetic Rayleigh and Love wave amplitude spectra and seismograms for the best-fitting focal mechanism and depth. For both the Rayleigh and Love waves there is reasonable agreement between the observed and synthetic amplitude spectra and in general there is also a good fit between the observed and synthetic seismograms.

For the 27^{th} August 2008 earthquake, while the observed surface wave amplitude spectra had a good SNR at regional and teleseismic distances, the data did not constrain the source depth. The

depth of this earthquake was however well constrained by the teleseismic depth phases (Figure 3) so a source mechanism and scalar moment were obtained by applying the Fox et al. (2012) method for a fixed depth of 11 km. All the focal mechanisms estimated using the surface wave amplitude spectra modelling are shown in Figure 6. With the exception of the 27^{th} August 2008 earthquake which is a strike-slip fault, all the source mechanisms are pure reverse faults. The surface-wave derived focal mechanisms are in good agreement with the GCMT solutions (2).

Uncertainty in the results of amplitude spectra modelling can be caused by noise in the data, errors in the Earth model used, and finite source effects. Fox et al. (2012) assumes that the cumulative impact of these has a Gaussian distribution and uses an F-test to determine the range of source parameters that can be considered statistically acceptable for a given earthquake. Generally the bounds placed on source depths estimated by modeling surface wave amplitude spectra are greater than for source depths estimated using depth phases provided the depth phases have been correctly identified. For the 3^{rd} September 2008 earthquake, source depths between 5 and 11 km are considered statistically acceptable within the 95% confidence bounds. A source depth of 11.7 ± 1.76 km was estimated using the teleseismic body waves for this earthquake therefore depths estimated by both methods are consistent. The surface wave depths are consistent with the teleseismic body wave depths for all six earthquakes where a depth has been estimated using both methods.

CALIBRATED EARTHQUAKE RELOCATION

Large systematic errors (10-15 km) in earthquake location in the Zagros region have been reported by numerous authors (e.g. Berberian, 1979; Elliott et al., 2015). In remote regions such as those where the 2008 and 2012 earthquake sequences occurred, such an epicentral uncertainty would prohibit the identification of the causative fault. To improve the location of the earthquakes we use Joint Epicentral Determination (JED) (Douglas, 1967) that simultaneously determines event location and station corrections. The station corrections account for lateral velocity variations that are neglected within the 1-D velocity model used to locate the event. The algorithm also includes Jeffreys' uniform reduction method (Jeffreys, 1932) to determine weights for each of the travel time observations at each iterative step of the location inversion. Uniform reduction assigns small weights for outliers (i.e. bad picks or phase mis-identification) and reduces their effect on the location.

Although this method improves relative location, to improve the absolute location we need information to fix either a specific seismic event or the centroid of the cluster. From the InSAR analysis we know the geometry and location of the slip on the fault plane, however, the best fitting slip distribution shows two asperities. Using observations of S-P times at an accelerometer located at Moosiyan (see Data and Resources section) we can constrain the location of the seismic event on the fault plane (Jackson et al. (2006) used a similar procedure to constrain the location of the 2003 Bam earthquake). The observations at Moosiyan show a clear S-P time of 2.9 s, which, for the upper crustal velocity structure in Masjed Soleyman (Dezful Embayment, (Nissen et al., 2011)) places the zone of rupture initiation at 21 km from the station. Knowing the depth of this event from the surface wave analysis (11 km) and the distance from the accelerometer at Moosiyan (21 km) we can locate the 27^{th} August 2008 event at the centre of the NW asperity in the slip model shown in Figure 2. We fix the location of the 2008 mainshock to the center of the NW asperity in the relocation procedure and the depths of events where we have independent estimates from depth analysis described above. This technique is similar to that described in in a number of recent studies, including several in Iran (e.g. Tatar et al., 2007; Bondár et al., 2008; Walker et al., 2013; Elliott et al., 2015).

Arrival time data from the REB, as well as from the two permanent networks in Iran, the Iran Seismograph Network operated by the International Institute for Seismology and Earthquake Engineering (IIEES) and the Iran Telemetered Seismograph Network operated by the Iran Seismological Research Center at the Institute of Geophysics of Tehran University (IGUT), were used in the relocation procedure. The regional phase readings from these Iranian networks allow us to better constrain the relative locations of events that are represented by teleseismic data. In total we relocate 89 events across the two sequences (Figure 6) with the seismicity clustering into two distinct groups ($\sim$35 km between them). The 2008 sequence lies on the Iran-Iraq border not close to any known or inferred faults. This cluster is more diffuse with no real structure, suggesting perhaps it generated very few aftershocks. Unfortunately, only two focal mechanisms could be calculated for this cluster. The main shock displays a strike-slip mechanism while the aftershock displays a thrust motion.

The 2012 events are further to the north-west and lie in close proximity to the ZFF. These events are much more clustered, still with some scatter, and two possible linear streaks within the

cluster that can be separated temporally. Further to the north-west is a cluster of events linked with seismicity between 28^{th} February and 19^{th} April (Figure 6 c)), whilst the second cluster is eastwards and includes the 20^{th} April event and the seismicity that followed (Figure 6 d)). In both clusters the main shock (the M_w 5.0 28^{th} February and the M_w 5.2 20^{th} April events) occur at the north-eastern edge of the cluster and the seismicity then propagates south-westwards. The two clusters also run perpendicular to the inferred trace of the ZFF. All of the focal mechanisms for the 2012 seismicity display similar pure thrust mechanisms.

It is always important to compare calibrated relocated seismicity with that presented in different seismic event catalogues. Such comparisons help determine the accuracy of the catalogue. The event locations and depths described in this study are compared to those reported in the REB, IGUT and IEES catalogues (Figure 7). The REB locations are generally more diffuse, with the events forming one cluster (the 2008 events are further westwards compared to the relocated events). The REB depths have been defined using only travel time data and not any depth phases. The majority of the REB events have fixed depths of 0 km, while the remaining events have depths $>$ 20 km. The IGUT events closely resemble those reported in this study, although again the events are generally located westwards of their actual position. The IGUT depths show a greater spread (2-32 km) than this study. The IIEES locations are very diffuse, with event depths at 14, 18 or $>$ 30 km. The IIEES station distribution in this region is sparse leading to the unreliable locations seen in this data set. The difference in location for 27^{th} of August 2008 event is: 9.2 km (REB), 14.5 km (IGUT) and 12.3 km (IIEES). The location difference for the 28^{th} February 2012 earthquake is: 12.5 km (REB), 16.3 km (IGUT) and 32.1 km (IIEES). While the location difference for the 20^{th} April 2012 event is: 16.2 km (REB), 10.72 km (IGUT) and 33.6 km (IIEES).

DISCUSSION

Strike-slip faulting in the SFB and accompanying aseismic deformation

Faulting in the SFB and particularly the Dezful Embayment is dominated by thrust faulting. The majority of previous work in this region of the Zagros focuses on thrust faulting, but the 27^{th} of August 2008 earthquake provides a rare opportunity to comment on how strike-slip faulting in the Zagros relates to the controversial topics of the depth distribution and relative role of seismic and aseismic

slip. Although only a moderately sized earthquake globally, in comparison to other seismicity in the SFB the magnitude of this event is significant. This was the second earthquake with this orientation close to the ZFF to occur in this region. The other earthquake was a M_w 5.3 event on the 18^{th} of June 2002 that occurred ∼150 km to the north-west, between the ZFF and MFF (Figure 1).

We used InSAR data covering the 27^{th} of August 2008 earthquake to obtain both a precise location of the event and model the orientation of the fault plane and slip. The location of the fault plane is ∼15 km north-east of the ZFF not close to previously known or inferred faults. The depth estimate from the InSAR and seismic modelling place this event in the sedimentary cover, with a centroid depth of ∼11 km. This suggests that like thrust events observed in this region (e.g. Talebian and Jackson, 2004; Nissen et al., 2011), strike-slip events rupture in the sedimentary cover and not the basement. The modelled slip occurred on a right-lateral fault (with a small thrust component, rake=158°), striking NW-SE and dipping steeply to the south-west. Global catalogs for this event reported a range of nodal plane orientations, but this ambiguity was resolved using both the results of our InSAR and surface wave modelling. Both the uniform and distributed slip geodetic models require a fault with length (∼40 km) significantly larger than expected for a M_w 5.8 earthquake (∼9km; Wells and Coppersmith (1994)), and a M_w ∼6 that corresponds to at least double the seismological estimates of moment release (Table 1).

The slip distribution in Figure 2g displays two interesting features: first, slip appears to terminate abruptly up-dip at a depth of around 6km along much of the fault's length and second, slip largely occurs as two discrete asperities, each of which are roughly equivalent to a M_w 5.8 earthquake (calculated over the two halves of the fault plane in Figure 2g that are separated by the dashed line). Slip takes place over a length of ∼40 km along-strike but is bounded at 6 km depth in the up-dip direction and 14km depth down-dip. The down-dip limit is at the depth where the basement is thought to be in this region, but slip at this depth is poorly resolved by our data (Figure 2g and Figure S6, available in the electronic supplement to this article). Whilst it is possible that a small amount of slip took place at depths <6 km (<∼3 cm), our uncertainties on the slip distribution along with smoothing and resolution tests (Figures 2g, Figure S5, available in the electronic supplement to this article, and Figure S6, available in the electronic supplement to this article) show that the shallow and abrupt termination of slip at ∼6 km is reasonably well resolved. Detailed stratigraphy in

the Dezful Embayment has shown numerous decoupling horizons within the sedimentary sequences between 3-9 km depth (Casciello et al., 2009). The slip distribution suggests the 27^{th} of August 2008 event propagated across a number of these horizons (including the Triassic Dashtak evaporites) but stopped at 6 km depth, where a detachment horizon linked with the Upper Cretaceous Gurpi-Pabdeh marls is observed. In fact only one of the aftershocks has a depth less than 6 km suggesting this detachment is an important barrier to seismogenic rupture or marks a boundary between seismogenic rocks and incompetent rocks.

The additional asperity and the extra seismic moment revealed in the InSAR modelling cannot be accounted for by the limited aftershock sequence. The summed moment of aftershocks listed in the IGUT catalog [this catalog has a magnitude of completeness of $\sim$3 for events in this region of Iran (Jafari, 2013)] in the interval covered by the SAR data is only $\sim$20% of the observed geodetic moment for the additional asperity. Larger moment release from geodetic results compared with seismological results is commonly reported in the Zagros (e.g. Lohman and Simons, 2005; Nissen et al., 2010; Roustaei et al., 2010) and elsewhere globally (e.g. Weston et al., 2011). The difference between the geodetic and seismological moments is usually attributed either to postseismic deformation contributing to the geodetic signal or to biases introduced by the choice of rheological crustal models. As described earlier, the elastic half-space parameters used in our geodetic inversion are consistent with those used by Nissen et al. (2011) to estimate moment using seismic body waves and are derived from a local estimate of the crustal velocity structure. In Table 1 we list various independently calculated moments using seismic observations (this study, GCMT, USGS BW, USGS UCMT and Nissen et al. (2011)). Although these moments have been calculated using different datasets, methods and Earth models they are all of comparable magnitude ($0.3 - 0.59 \times\ 10^{18}$ Nm). As it is well-known that there is a trade-off between source depth and scalar moment for seismological source models, we examined the possibility for our seismic model of the 27^{th} of August 2008 earthquake that the source is at 22 km depth (twice the source depth estimated using the teleseismic body waves) and consequently has a larger scalar moment. Even with the source at a depth of 22 km, the resulting upper limit on the scalar moment is $0.50 \times\ 10^{18}$ Nm. All these seismic estimates of moment are $\sim$20-50% of the geodetic moment estimate, even when taking into account the uncertainty in the geodetic moment (the uniform model geodetic moment is $1.4 \pm 0.2 \times\ 10^{18}$ Nm, Table 1). The use

of half-space crustal models rather than those that incorporate more realistic elastic layering can also bias estimates of moment from geodetic data (Cattin et al., 1999; Hearn and Burgmann, 2005). For strike-slip faults, however, the half-space simplification leads to an underestimation of geodetic moment (Hearn and Burgmann, 2005) and therefore incorporation of elastic layering would only increase our discrepancy between seismic and geodetic moment. Overall, these considerations suggest that Earth model variation or InSAR data uncertainties cannot explain the difference between the geodetic and seismological moment estimates and that postseismic deformation is the more likely explanation. It is not without precedent for InSAR-derived estimates of moment to be higher than seismic estimates by a factor of two or more for both strike-slip and thrust earthquakes (Weston et al., 2012). The largest discrepancies between seismic and geodetic moment for strike-slip earthquakes globally have been attributed to poor or noisy InSAR data (Weston et al., 2012), including for the 1994 Al Hoceima strike-slip earthquake in Morocco (Biggs et al., 2006) where the geodetic moment is estimated to be somewhere between 70% greater than and triple the seismic moment. However, for thrust earthquakes, aseismic slip has commonly been proposed to explain major discrepancies between geodetic and seismic moment, and there are many examples in particular from the Zagros in Iran.

Seismic moment tensors for the past century cannot account for geodetically measured convergence of the Arabian and Eurasian plates (Jackson and McKenzie, 1988), implying that aseismic shortening is significant in the Zagros. For the 2005 M_w 5.8 Qeshm Island earthquake, the InSAR-derived moment is double the estimate from body-wave modelling (Nissen et al., 2010), and for the 2006 Fin earthquake sequence, of which the largest event was M_w 5.7, the geodetic estimate is 50% higher than the body-wave estimate (Roustaei et al., 2010). Lohman and Simons (2005) found geodetic moments up to six times higher than moments from the GCMT and ISC catalogues for a number of small ($M_w \leq 5.1$) earthquakes in the Zagros, and aseismic slip with moment release equivalent to M_w 5.7 has been inferred to follow the M_w 6.1 2013 Khaki-Shonbe earthquake respectively (Elliott et al., 2015). In the Khaki-Shonbe example, the aseismic slip patch was inferred to have occurred along strike from the seismic asperity. We suggest that the InSAR data for the 27^{th} August 2008 earthquake reflect a similar case, albeit for a strike-slip fault. We propose that only the NW asperity ruptured seismically, accounting for the seismic M_w of 5.8, and the other asperity slipped

aseismically at some point between the 27^{th} of August 2008 earthquake and the 9^{th} of April 2009, the earliest of our post-seismic SAR acquisitions. Our study therefore provides the first evidence that aseismic slip is important not only on thrust faults but also on strike-slip faults in the Zagros. Aseismic deformation in Iran, manifesting either as slow earthquakes or as post-seismic deformation, has variously been suggested to occur either in the basement (Barnhart and Lohman, 2013), at shallower levels within the sediment (e.g. Copley and Reynolds, 2014) or on sections of the ruptured fault with a lack of aftershock observations (e.g. Elliott et al., 2015). Here we find is no evidence for depth separation of the regions of seismic and aseismic slip as has been debated for thrust faults located in the Zagros Simply Folded Belt (e.g. Barnhart and Lohman, 2013; Nissen et al., 2014).

The oblique convergence between Arabia and Iran requires some right-lateral motion and analysis of GPS crustal velocities indicate that not all of this motion is accommodated in the High Zagros by the MRF (Walpersdorf et al., 2006). It has been previously postulated (Nissen et al., 2011) that some percentage of the right-lateral deformation occurs along the ZFF deformation front. The location, size and mechanism of the 27^{th} of August 2008 earthquake provide observational evidence that some of this motion is accommodated in the vicinity of the ZFF, both seismically and aseismically.

Seismogenic movement of the ZFF or a new fault?

The majority of the 2012 events lie in close proximity to the ZFF. In particular, they form two clusters that are aligned perpendicular to the trend of the ZFF and can be separated both temporally and spatially (seismicity between 28^{th} February and 19^{th} April and seismicity observed after 20^{th} April 2012). Both of these clusters start with the largest magnitude event in the cluster (the M_w 5.0 28^{th} February and the M_w 5.2 20^{th} April events) and then the seismicity propagates towards the south-west. The focal mechanisms for both clusters are consistent, displaying pure thrust mechanisms. These clusters suggest either a single thrust fault (perhaps a continuation of the ZFF into the overlying sediment, although Berberian (1995) describes the ZFF as a purely basement fault) or two thrust faults in close proximity. If it is indeed a single fault in this region, the two clusters indicate that two different sections of the fault ruptured, the first starting on the 28^{th} February 2012 before migrating south-west and upwards towards the surface. This possibly triggered a second section of the fault to rupture, $\sim$10 km eastwards, again starting deeper and migrating towards the south-west and

shallower. An alternative interpretation is that two unknown faults in this location created the two seismicity clusters. The fact that the majority of faults in this region are blind and cannot be mapped at the surface, and that this region has had a previous lack of observed seismicity (Figure 1) makes it difficult to distinguish between the two.

Depth distribution of Seismogenic faulting

A long standing problem within the Zagros is the depth extent of faulting and whether faults penetrate deep enough to cut the basement. Some authors propose significant basement involvement (Jackson, 1980), while others promote complete basement detachment (McQuarrie, 2004). To date no earthquake in the SFB has been known to generate a surface rupture. Teleseismic data (Maggi et al., 2000; Engdahl et al., 1998) and local dense temporary seismic networks across the Zagros (e.g. Hatzfeld et al., 2003; Nissen et al., 2011; Yaminifard et al., 2012) suggest that most seismicity occurs at depths of 10-25 km within the uppermost portion of Arabian plate basement. Recently, Barnhart and Lohman (2013) suggested that InSAR observations from larger earthquakes in the Zagros are not generated by the main shock itself but by aseismic slip within the overlying sediment cover, with the main shock actually occurring in the basement. They propose that seismic strain is being released by shortening of the basement, with aseismic slip in the overlying sediments playing an important role.

Conversely, other InSAR studies in the Zagros (e.g. Lohman and Simons, 2005; Nissen et al., 2007) and teleseismic body-waveform modeling studies (e.g. Talebian and Jackson, 2004; Nissen et al., 2011) support reverse faulting earthquakes located in the mid- or lower sedimentary cover (4-10 km depth). Aftershocks following two such events have been located at greater depths in the basement and do not overlap with the inferred fault slip (e.g. Nissen et al., 2010; Roustaei et al., 2010). These observations suggest the majority of the seismic strain is released within the 'Competent Group' within the lower sedimentary cover and the interleaving salt layers may limit earthquake size by inhibiting rupture propagation between the cover and basement (e.g. Nissen et al., 2011).

Unusually for seismicity in the Zagros and the SFB, we report on both thrust and strike-slip events in two separate sequences. We use a combination of surface wave inversions and teleseismic body wave observations to independently determine event depths, and in some cases we have used

both techniques to determine an event depth, with consistent results. The majority of the event depths in this study are between 6-10 km, with a few events at depths of 12 km. The depth of the basement in this region is not known specifically, but is thought to be at $\sim$13 km. This places the main shock for each cluster and the aftershocks well within the sedimentary cover, with perhaps a few events close to the basement. The geodetic slip distribution for the 27^{th} August 2008 event shows slip patches between 6-14km depth, suggesting that slip is inhibited from migrating into the basement. This suggests that faults in this region of the Zagros, both thrust and strike-slip, either do not penetrate into the basement or are not seismically active at such depths. The up-dip extent of the slip distribution for the 27^{th} August 2008 event and the fact that depths to all the events in this study are generally $>$6 km suggest a possible decoupling horizon at this depth plays a significant role in the migration of slip and deformation in the sedimentary cover.

CONCLUDING REMARKS

Using a combination of geodetic and seismological information we analyse three earthquakes (a M_w 5.8 on the 27^{th} August 2008, a M_w 5.0 on the 28^{th} February 2012 and a M_w 5.2 on the 20^{th} April 2012) and their aftershock sequences on the border between Iran and Iraq. InSAR data were inverted to find both the geometry and the distribution of slip on the fault plane for the 27^{th} August 2008 event. The inversion provides a well-determined fault plane geometry that is consistent with seismological solutions, but the geodetic moment is much larger than estimates of seismic moment, most likely due to significant triggered asesimic slip. There is no evidence for depth separation between the proposed seismic and aseismic slip as has been previously proposed and debated for thrust faults in the region (e.g. Barnhart and Lohman, 2013; Nissen et al., 2014). Using a combination of body-wave and surface wave teleseismic observations we estimate depths (4 - 13 km) for 36 earthquakes within the aftershock sequences. When compared to the known stratigraphy of the region, these depths suggest the events are located within the sedimentary cover and not the underlying basement. This suggests that like thrust events in this region, strike-slip events also take place in the sedimentary cover rather than the basement.

The joint epicentral determination technique was applied to the 2008 and 2012 sequences, using the InSAR observations to fix the 27^{th} August 2008 location. The seismicity splits into three separate

clusters linked to the three main events. The 2008 sequence has limited aftershock activity and displays a diffuse pattern with little internal structure. This is perhaps surprising given the size of the earthquake, but again suggests that aseismic deformation plays a key role during deformation in this region. The 2012 seismicity separates into two distinct clusters, located in close proximity to the ZFF and suggest that this region is not completely aseismic. Further to the north-west are events linked with seismicity between 28^{th} February and 19^{th} April, whilst the second cluster is eastwards and includes the 20^{th} April event and the seismicity that followed. In both clusters the main shock (the M_w 5.0 28^{th} February and the M_w 5.2 20^{th} April events) occurs at the north-eastern edge of the cluster and the seismicity then propagates south-westwards. The close spatial and temporal proximity between the two clusters suggests that either two portions of the same fault ruptured separately or two individual faults created the seismicity. In both scenarios it is likely the second event (M_w 5.2 20^{th} April) and its aftershocks may have been triggered by the M_w 5.0 28^{th} February earthquake and its aftershock sequence.

Analysis of the 27^{th} August 2008 event provides us with valuable insights into deformation processes in this part of the Zagros. First, it provides us with the location of a previously unknown strike-slip fault in this region. Second, it demonstrates that aseismic slip plays an important role not only for thrust faults but also for strike-slip faults in the Zagros. Finally, GPS velocities across the Main Recent Fault suggest the slip rate on this fault is not sufficient to accommodate all of the right-lateral component of the Arabia-Iran motion (Walpersdorf et al., 2006) and the occurrence of the 27^{th} August 2008 strike-slip earthquake suggests that significant right-lateral deformation may occur either along or in close proximity to the ZFF deformation front. Further seismicity and geodetic measurements are required to fully understand the nature, geometry and effect the ZFF has on deformation in this region.

DATA AND RESOURCES

Figures were prepared using GMT Wessel and Smith (1995). All ENVISAT SAR data are copyrighted by the European Space Agency and were provided to RJW under project C1P.13911. We are grateful to JPL/Caltech for use of the ROI_PAC software. REB arrival time data and event locations were obtained from the ISC catalog using

www.isc.ac.uk/iscbulletin/search/catalogue (last accessed September 2016). The IIEES arrival time data and event locations were obtained from the International Institute of Earthquake Engineering and Seismology website www.iiees.ac.ir (last accessed September 2016). The IGUT arrival time data and event locations were obtained from the Iranian Seismological Center website irsc.ut.ac.ir/bulletin.php (last accessed September 2016). The strong motion waveform recorded at Moosiyan by the Road, Housing and Urban Development Research Centre was obtained from ismn.bhrc.ac.ir (last accessed September 2016). The seismic waveform data was obtained from the IRIS website, www.iris.edu (last accessed August 2015) or from the CTBTO International Data Centre. The Global Centroid Moment Tensor database was searched using
www.globalcmt.org/CMTsearch.html (last accessed August 2015). The USGS moment tensor solutions were obtained from the ISC catalog using
www.isc.ac.uk/iscbulletin/search/catalogue (last accessed August 2015).

ACKNOWLEDGMENTS

This work was partially supported by the National Environment Research Council and the Economic and Social Research Council through grant NE/J02001X/1 and by the Natural Environment Research Council (NERC) through the Centre for the Observation and Modelling of Earthquakes, Volcanoes and Tectonics (COMET). We thank three anonymous reviewers for their insightful comments.

REFERENCES

Aki, K., and P.G. Richards (1980). *Quantitative Seismology*. New York: Freeman.

Allen, M.B., and M. Talebian (2011). Structural variation along the Zagros and the nature of the Dezful Embayment, *Geophys. J. Int.* **148**, 911–924, doi:10.1017/S0016756811000318.

Barnhart, W.D., and R.B. Lohman (2013). Phantom earthquakes and triggered aseismic creep: Vertical partitioning of strain during earthquake sequences in Iran, *Geophys. Res. Lett.* **40**, 819–823, doi:10.1002/grl.50201.

Berberian, M. (1979). Evaluation of instrumental and relocated epicentres of Iranian earthquakes, *Geophys. J. R. astr. Soc.* **58**, 625–630.

617 Berberian, M. (1995). Master blind thrusts faults hidden under the Zagros folds: active basement
618 tectonics and surface morphotectonics, *Tectonophysics* **241**, 193–224.
619 Biggs, J., E. Bergman, B. Emmerson, G.J. Funning, J. Jackson, B. Parsons, and T.J. Wright (2006).
620 Fault identification for buried strike-slip earthquakes using InSAR:The 1994 and 2004 Al Hoceima,
621 Morocco earthquakes, *Geophys. J. Int.* **166**, 1347–1362.
622 Bondár, I., E. Bergman, E.R. Engdahl, B. Kohl, Y.-L. Lung, and K. McLaughlin (2008). A Hybrid
623 Multiple Event Location Technique to Obtain Ground Truth Event Locations, *Geophys. J. Int.* **175**,
624 185–201.
625 Casciello, E., J. Vergés, E. Saura, G. Casini, N. Fernández, E. Blanc, S. Homke, and D.W. Hunt
626 (2009). Fold patterns and mulitlayer rheology of the Lurestan Province, Zagros Simply Folded Belt
627 (Ian), *J. Geol. Soc.* **166**, 947–959, doi:10.1144/0016-76492008-138.
628 Cattin, R., P. Briole, H. Lyon-Caen, P. Bernard, and P. Pinettes (1999). Effects of superficial layers
629 on coseismic displacements for a dip-slip fault and geophysical implications, *Geophys. J. Int.* **137**,
630 149–158.
631 Copley, A., and K. Reynolds (2014). Imaging topographic growth by long-lived post-seismic afterslip
632 at Sefidabeh, east Iran, *Tectonics* **33**, 330–345, doi:10.1002/2013TC003462.
633 Douglas, A., (1967). Joint Epicentre Determination, *Nature* **215**, 47–48.
634 Ekström, G., M. Nettles, and A.M. Dziewoński (2012). The global CMT project 2004-2010:
635 Centroid-moment tensors for 13,017 earthquakes, *Phys. Earth Planet. Inter.* **200–201**, 1–9,
636 doi:10.1016/j.pepi.2012.04.002.
637 Elliott, J.R., E.A. Bergman, A.C. Copley, A.R. Ghods, E.K. Nissen, B. Oveisi, M. Tatar, R.J.
638 Walters, and F. Yamini-Fard (2015). The 2013 Mw 6.2 Khaki-Shonbe (Iran) Earthquake: in-
639 sights into seismic and aseismic shortening of the Zagros sedimentary cover, *Earth and Space Sci.*
640 doi:10.1002/2015EA000098.
641 Engdahl, E.R., R.D. van der Hilst, and R. Buland (1998). Global teleseismic earthquake relocation
642 from improved travel times and procedures for depth determination, *Bull. Seismol. Soc. Am.* **88**,
643 722–743.
644 Farr, T., P.A. Rosen, E. Caro, R. Crippen, R. Duren, S. Hensley, M. Kobrick, M., Paller, E.
645 Rodriguez, L. Roth, D. Seal, S. Shaffer, S. Shimada, J. Umland, M. Werner, M. Oskin, D.

646 Burbank, and D. Alsdorf (2007). Shuttle Radar Topography Mission, *Rev. Geophys.* **45**,(2),
647 doi:10.1029/2005RG000183.
648 Fox, B.D., N.D. Selby, R. Heyburn, and J.H. Woodhouse (2012). Shuttle Radar Topography Mission,
649 *Geophys. J. Int.* **191**,601–615.
650 Funning, G.J., B. Parsons, T.J. Wright, J.A. Jackson, and E.J. Fielding (2005). Surface displacements
651 and source parameters of the 2003 Bam (Iran) earthquake from Envisat advanced synthetic aperture
652 radar imagery, *J. Geophys. Res.* **110**,(B9), doi:10.1029/2004JB003338.
653 Goldstein, R.M. and C.L. Werner (1998). Radar interferogram filtering for geophysical applications,
654 *Geophys. Res. Lett.* **25**, 4035–4038, doi:10.1029/1998GL900033.
655 Hatzfeld, D., M. Tatar, K. Priestley, and M. Ghafory-Ashtiany (2003). Seismological constraints
656 on the crustal structure beneath the Zagros Mountain belt (Iran), *Geophys. J. Int.* **155**,403–410,
657 doi:10.1046/j.1365-246X.2003.02045.x.
658 Hearn, E.H. and R. Burgmann (2005). The Effect of Elastic Layering on Inversions of GPS Data for
659 Coseismic Slip and Resulting Stress Changes: Strike-Slip Earthquakes, *Bull. Seismol. Soc. Am.* **95**,
660 1637–1653, doi:10.1785/0120040158.
661 Herrin, E. and T. Goforth (1977). Phase-matched filters: Application to the study of Rayleigh waves,
662 *Bull. Seismol. Soc. Am.* **67**, 1259–1275.
663 Jackson, J., (1980). Reactivation of basement faults and crustal shortening in orogenic belts, *Nature*
664 **283**, 343–346, doi:10.1038/283343a0.
665 Jackson, J. and D. McKenzie (1988). The relationship between plate motions and seismic moment
666 tensors, and the rates of active deformation in the Mediterranean and Middle East, *Geophys. J.*
667 *Int.* **93**, 45–73, doi:10.1111/j.1365-246X.1988.tb01387.x.
668 Jackson, J., M. Bouchon, E. Fielding, G. Funning, M. Ghorashi, D. Hatzfeld, H. Nazari, B. Parsons,
669 K. Priestley, M. Talebian, M. Tatar, R. Walker, and T. Wright (2006). Seismotectonic, rupture
670 process, and earthquake-hazard aspects of the 2003 December 26 Bam, Iran, earthquake, *Geophys.*
671 *J. Int.* **166**, 1270–1292, doi: 10.1111/j.1365-246X.2006.03056.x.
672 Jafari, M.A., (2013). Spatial distribution of seismicity parameters in the Persian Plateau, *Earth*
673 *Planets Space* **65**, 863–869.
674 Jeffreys, H., (1932). An alternative to the rejection of observations, *Proc. R. Soc. Lond.* **187**, 78–87.

675 Jónsson, S., H. Zebker, P. Segall, and F. Amelung (2002). Fault slip distribution of the M_w 7.2
676 Hector Mine earthquake estimated from satellite radar and GPS measurements, *Bull. Seismol. Soc.*
677 *Am.* **94**,(92), 1377–1389, doi:10.1785/0120000922.
678 Lohman, R.B., and M. Simons (2005). Locations of selected small earthquakes in the Zagros moun-
679 tains, *Geochem. Geophys. Geosyst.* **6**, Q03001, doi:10.1029/2004GC000849.
680 Maggi, A., J.A. Jackson, K. Priestley, and C. Baker (2000). A re-assessment of focal depth distri-
681 butions in southern Iran, the Tien Shan and northern India: do earthquakes really occur in the
682 continental mantle?, *Geophys. J. Int.* **143**, 629–661.
683 Masson, F., J. Chéry, D. Hatzfeld, J. Martinod, P. Vernant, F. Tavakoli, and M. Ghafory-Ashtiani
684 (2005). Seismic versus aseismic deformation in Iran inferred from earthquakes and geodetic data,
685 *Geophys. J. Int.* **160**, 217–226, doi:10.1111/j.1365-246X.2004.02465.x.
686 McQuarrie, N., (2004). Crustal scale geometry of the Zagros fold-thrust belt, Iran, *J. Struct. Geol.*
687 **26**, 519–535.
688 Morris, P., (1977). Basement structure as suggested by aeromagnetic surveys in southwest Iran,
689 *Internal report, Oil Serivce Company of Iran*.comparison with the Himalayas, J. geophys. Res.,
690 91(B8), 8205–8218.
691 Motagh, M., A. Bahroudi, M.H. Haghighi, S. Samsonov, E. Fielding, and H-U. Wetzel (2015). The 18
692 August 2014 Mw6.2 Mormori, Iran, earthquake: A Thin-skinned faulting in the Zagros Mountain
693 inferred from InSAR measurements, *Seis. Res. Lett.* **86**,(3), 775–782, doi:10.1785/0220140222.
694 Nissen, E., M. Ghorashi, J.A. Jackson, P. Parsons, and M. Talebian (2007). The 2005 Qeshm Island
695 earthquake (Iran) – a link between buried reverse faulting and surface folding in the Zagros Simply
696 Folded Belt?, *Geophys. J. Int.* **171**, 326–338.
697 Nissen, E., F. Yamini-Fard, M. Tatar, A. Gholamzadeh, E. Bergman, J.R. Elliott, J.A. Jackson, and
698 B. Parsons (2010). The vertical separation of mainshock rupture and microseismicity at Qeshm
699 island in the Zagros Simply Folded Belt, Iran, *Earth planet. Sci. Lett.* **296**, 181–194.
700 Nissen, E., M. Tatar, J.A. Jackson, and M.B. Allen (2011). New views on earthquake faulting
701 in the Zagros fold-and-thrust belt of Iran, *Geophys. J. Int.* **186**, 928–944, doi:10.1111/j.1365-
702 246X.2011.05119.x.
703 Nissen, E., J. Jackson, S. Jahani, and M. Tatar (2014). Zagros "phantom earthquakes" reassessed

- The interplay of seismicity and deep salt flow in the Simply Folded Belt?, *J. Geophys. Res.* **119**, (4), 3561–3583, doi:10.1002/2013JB010796.

O'Brien, C.A.E., (1957). Salt diapirism in south Persia, *Geologie en Mijnbouw* **19**, 357–376.

Okada, Y., (1985). Surface deformation due to shear and tensile faults in a half-space, *Bull. Seismol. Soc. Am.* **75**,(4), 1135–1154.

Patton, H., (1998). Bias in the centroid moment tensor for central Asian earthquakes: evidence from regional surface wave data, *J. Geophys. Res.* **103**,26963–26974.

Rosen, P.A., S. Hensley, G. Peltzer, and M. Simons (2004). Update Repeat Orbit Interferometry Package Released, *Eos Trans. AGU* **85**, 47–47, doi:10.1029/2004EO050004.

Roustaei, M., E. Nissen, M. Abbassi, A. Gholamzadeh, M. Ghorashi, M. Tatar, F. Yamini-Fard, E. Bergman, J. Jackson, and B. Parsons (2010). The 25 March 2006 Fin earthquakes (Iran) – insights into the vertical extents of faulting in the Zagros Simply Folded Belt, *Geophys. J. Int.* **181**, 1275–1291, doi:10.1111/j.1365-246X.2010.04601.x.

Shapiro, N.M., and M.H. Ritwoller (2002). Monto-Carlo inversion for global shear-velocity model of the crust and upper mantle, *Geophys. J. Int.* **151**, 81–105.

Stein, S., and D. A. Wiens (1986). Depth determination for shallow teleseismic earthquakes, *Rev. Geophys.* **24**, 806–832.

Talebian, M., and J. Jackson (2004). A reapprasial of earthquake focal mechanisms and active shortening in the Zagros mountains of Iran, *Geophys. J. Int.* **156**, 506–526.

Tatar, M., J. Jackson, D. Hatzfeld, and E. Bergman (2007). The 2004 May 28 Baladeh earthquake (Mw 6.2) in the Alborz, Iran: overthrusting the South Caspian Basin margin, partitioning of oblique convergence and the seismic hazard of Tehran, *Geophys. J. Int.* **170**, 249-261, 10.1111/j.1365-246X.2007.03386.x

Tsai, Y.B., and K. Aki (1970). Precise focal depth determination from amplitude spectra of surface waves, *J. Geophys. Res.* **75**, 5729–5743.

Vernant, P., F. Nilforoushan, D. Hatzfeld, M.R. Abbassi, C. Vigny, F. Masson, H. Nankali, J. Martinod, A. Ashtiani, R. Bayer, F. Tavakoli, and J. Cheŕy (2004). Present-day crustal deformation and plate kinematics in the Middle East constrained by GPS measurements in Iran and northern Oman, *Geophys. J. Int.* **157**, 381–398, doi:10.1111/j.1365-246X.2004.02222.x.

733 Walker, R.T., E. Bergman, J.R. Elliott, E.J. Fielding, A.-R. Ghods, M. Ghoraishi, J. Jackson, H.
734 Nazari, M. Nemati, B. Oveisi, M. Talebian, and R.J. Walters (2013). The 2010–2011 South Rigan
735 (Baluchestan) earthquake sequence and its implications for distributed deformation and earthquake
736 hazard in southeast Iran, *Geophys. J. Int.* **193**, 349–374, doi:10.1093/gji/ggs109.

737 Walpersdorf, A., D. Hatzfeld, H. Nankali, F. Tavakoli, F. Nilforoushan, M. Tatar, P. Vernant, and
738 J. Cheŕy, and F. Masson (2006). Difference in the GPS deformation pattern of North and Central
739 Zagros (Iran), *Geophys. J. Int.* **167**,(3), 1077–1088, doi:10.1111/j.1365-246X.2006.03147.x.

740 Wells, D.L. and K.J. Coppersmith (1994). New empirical relationships among magnitude, rupture
741 length, rupture width, rupture area, and surface displacement, *Bull. Seismol. Soc. Am.* **84**,(4),
742 974–1002.

743 Wessel, P. and W.H.F. Smith (1995). New version of the Generic Mapping Tools released, *EOS,*
744 *Trans. Am. geophys. Un.* **76**, 329.

745 Weston, J., A.M.G. Ferreira, and G.J. Funning (2011). Global compilation of interferometric synthetic
746 aperture radar earthquake source models: 1. Comparisons with seismic catalogs, *J. Geophys. Res.*
747 **116**, B08408, doi:110.1029/2010JB008131.

748 Weston, J., A.M.G. Ferreira, and G.J. Funning (2012). Systematic comparisons of earth-
749 quake source models determined using InSAR and seismic data, *Tectonophysics* **532**, 61–81,
750 doi:10.1016/j.tecto.2012.02.001.

751 Wright, T.J., Z. Lu, and C. Wicks (2003). Source model for the M_w 6.7, 23 October
752 2002, Nenana Mountain Earthquake (Alaska) from InSAR, *Geophys. Res. Lett.* **30**,(18),
753 doi:10.1029/2003GL018014.

754 Yaminifard, F., M. Hassanpour Sedghi, A. Gholamzadeh, M. Tatar, and K. Hessami (2012). Af-
755 ter shock analysis of the 2005 November 27 (M_w 5.8) Qeshm Island earthquake (Zagros-Iran):
756 Triggering of strike-slip faults at the basement, *J. Geodyn.* **55**,56–65.

AUTHOR AFFILIATIONS

Stuart E.J. Nippress and Ross Heyburn
AWE Blacknest,
Brimpton,
Reading,
U.K.
stuart@blacknest.gov.uk
ross@blacknest.gov.uk

R.J. Walters
COMET,
School of Earth & Environment,
University of Leeds,
Leeds,
LS2 9JT,
U.K.

Now at:
COMET,
Department of Earth Sciences,
Durham University,
Durham,
DH1 3LE,
U.K.
richard.walters@durham.ac.uk

FIGURE CAPTIONS

Figure 1. Topographic map (SRTM) of the north-western Zagros showing the major faults in the region (Nissen et al., 2011), population centers, and fault plane solutions for all M_w>4.6 earthquakes occurring in the last 25 years listed in the Global CMT catalog. The 2008 and 2012 fault plane solutions from the Global CMT are also shown (gray focal mechanisms). Major active faults are shown by the black lines and are dashed if they are blind. DEF, Dezful Embayment Fault; HZF, High Zagros Fault; MFF, Mountain Front Fault; MRF, Main Recent Fault; MZRF, Main Zagros Reverse Fault; ZFF, Zagros Foredeep Fault. Dotted lines show other potential major faults, including the Balarud Line. The border between Iran and Iraq is shown by the dotted and dashed line. The white box indicates the region of interest in this study and the area shown in Figures 6 and 7. Globe to the right shows the location of the study area.

Figure 2. InSAR data and elastic dislocation model for the 27^{th} August 2008 earthquake. (a) Stack of two descending track ENVISAT SAR interferograms spanning the intervals 23^{rd} of February 2006 to 22^{nd} of July 2010 and 15^{th} of November 2007 to 4^{th} of March 2010. Black arrows show the flight direction of ENVISAT (Az), the line-of-sight direction (los) and the incidence angle at the center of the interferogram (i). (b) Best-fitting elastic dislocation model for the distributed slip solution (Table 1), obtained from the joint inversion of both ascending and descending track InSAR data. The solid black line shows the surface trace of the uniform slip solution (Table 1), whilst the dashed black rectangle shows the surface projection of the distributed slip fault plane shown in (g). (c) Residuals between the data and the model. (d), (e) and (f) are the same as (a), (b) and (c) but for a single ascending track ENVISAT interferogram spanning the interval 25^{th} of January 2007 to 9^{th} of April 2009. (g) Best-fitting slip distribution on the fault plane from the distributed slip model, and associated 2 sigma uncertainties. Green circle shows the location of the 27^{th} August 2008 earthquake using observations recorded by an accelerometer located in Moosiyan (see section 7 of the text). (h) Digital elevation model for the same area shown in (a)–(f).

Figure 3. (a) Selected SP teleseismic *P* seismograms recorded for the 27 August 2008 m_b5.0 earthquake. Seismograms have been bandpass filtered with a passband of 1.0-2.5 Hz at KEST, 1.25-3.0 Hz at SCHQ, 1.75-3.5 Hz at HFS, 1.25-3.0 Hz at NOA, 2.0-4.0 Hz at EKA and 1-3.0 Hz at INK.

The phases interpreted as *P* and *pP* are labelled on the seismograms and *P* arrives at zero seconds at all stations. (b) Location map showing the epicentre of the 27 August 2008 m_b5.0 earthquake and selected stations used in the teleseismic body wave analysis.

Figure 4. (a) Lower hemisphere stereographic projections of focal mechanisms which best-fit the observed surface wave amplitude spectra at each grid-searched depth for the 3^{rd} September 2008 earthquake. Misfits are normalized using the lowest value of the least squares of the misfit between the observed and synthetic surface wave amplitude spectra. (b) Location map showing stations used to estimate the source mechanism and depth of the 3^{rd} September 2008 earthquake.

Figure 5. Observed (black dotted lines) and synthetic (gray lines) Rayleigh (a) and Love (b) wave amplitude spectra and filtered waveforms (100-30 s) for our preferred source mechanism and depth for the 3^{rd} September 2008 Iran earthquake. For each station the amplitude spectra are plotted above the waveforms.

Figure 6. (a) Relocated events with their 90 per cent confidence ellipses. The dotted and dashed line represents the Iran-Iraq border. The solid black line shows the surface trace of the uniform slip solution, whilst the dashed black rectangle shows the surface projection of the distributed slip fault plane. The inferred locations of the MFF, ZFF and the Balarud Line are also shown (after Nissen et al. (2011)). Relocated events and lower hemisphere stereographic projections of focal mechanisms estimated for the 2008 and 2012 earthquakes analyzed here. (b) Black circles represent the relocation of the 2008 seismicity, (c) black circles are events observed between 28^{th} February 2012 and 19^{th} April 2012, and (d) black circles represent the earthquake on the 20^{th} April 2012 and the seismicity that followed. The focal mechanisms have black quadrants to show positive (compressional) P polarity and are scaled by magnitude. 1 indicates the focal mechanism for the 27^{th} August 2008 earthquake, 2 the focal mechanism for the 28^{th} February 2012 earthquake and 3 indicates the mechanism for the 20^{th} April 2012 earthquake.)

Figure 7. Comparison of location and depths of events in the 2008 and 2012 sequences with those reported in the REB, IGUT and IIEES catalogs. Top Panel: Locations in the REB (left), IGUT (middle) and IIEES (right) catalogs. White circles are the locations for the 2008 sequence, while black circles are the 2012 locations. The dotted and dashed line represents the Iran-Iraq border. The solid black line shows the surface trace of the uniform slip solution, whilst the dashed black rectangle

shows the surface projection of the distributed slip fault plane. The inferred locations of the MFF, ZFF and the Balarud Line are also shown (after Nissen et al. (2011)). Bottom Panel: Comparison of depths calculated in this study with depths from the REB (left), IGUT (middle) and IIEES (right) catalogs.

Table 1. Source Parameters for the 2008/08/27 earthquake from various sources.

Model[a]	Strike °	Dip °	Rake °	Focal Sphere	Slip m	Lon[b] °	Lat[b] °	Length km	Top km	Bottom km	Centroid km	Moment $\times 10^{18}$ Nm	M_w
InSAR-u	141 ± 4[c]	61 ± 7[c]	158 ± 6[c]		0.9 ± 0.64[c]	47.5502 ± 1.2km[c]	32.2949 ± 2.0km[c]	43.9 ± 2.9[c]	8.5 ± 1.0[c]	10.1 ± 1.7[c]	9.3 ± 0.8[c]	1.42 ± 0.20[c]	6.04
InSAR-d	141[d]	61[d]	158[d]		-	47.5502	32.2949	60	0	20	10.8	1.70	6.09
SW	157	86	145		-	47.415	32.354				13.0	0.38	5.71
GCMT	338	85	-174		-	47.350	32.308	-	-	-	12.5	0.59	5.8
USGS BW	158	88	176		-	47.350	32.308	-	-	-	14	0.40	5.7
USGS UCMT	336	60	163		-	47.350	32.308	-	-	-	10	0.47	5.7
Nissen et al.	338	88	-168		-	47.35	32.31	-	-	-	10	0.30	5.6

[a]GCMT, Global Centroid Moment Tensor (Ekström et al., 2012); USGS UCMT, USGS Centroid Moment Tensor Solution; SW, surface waveform model from this study; InSAR-u, uniform elastic dislocation InSAR model, using values of $\lambda = \mu = 2.06 \times 10^{10}$ Pa for elastic Lamé' parameters; InSAR-d, distributed-slip InSAR model; Nissen et al., values from Nissen et al. (2011). Only the NNW striking nodal plane is presented for all models, as the nodal plane ambiguity is resolved by our InSAR models.

[b]Location given as hypocentre for seismic models, and as the up-dip projection of the centre of the fault plane for InSAR models.

[c]Formal 1σ errors of model fault parameters determined using a Monte Carlo method (e.g. Wright et al., 2003). See Figure S4 for full uncertainties and trade-offs.

[d]Values fixed at those from uniform slip model.

Table 2. Calibrated earthquake locations in the study region determined using the JED method.

Date	Time (UTC)	Lat. (°N)	Long. (°E)	Depth (km)	m_b	m_w	ϕ_s(°)	δ(°)	λ(°)	Method
2008/08/27	21:52:38.78	32.354	47.415	11.00*	5.0	-	250	55	5	SW
				12.5	5.3	5.8	247	84	-5	CMT
2008/08/27	23:04:12.53	32.379	47.324	11.30*	3.8	-	-	-	-	-
2008/08/28	00:13:44.38	32.273	47.437	-	-	-	-	-	-	-
2008/09/03	22:43:13.23	32.333	47.330	9.00	4.7	-	310	40	95	SW
				12.0	5.1	5.1	294	34	78	CMT
2008/09/03	23:14:43.03	32.361	47.367	12.90*	4.0	-	-	-	-	-
2008/09/04	08:42:45.53	32.394	47.327	9.85*	3.7	-	-	-	-	-
2008/09/06	23:53:29.45	32.335	47.359	-	4.2	-	-	-	-	-
2008/09/07	04:43:09.99	32.402	47.339	-	3.8	-	-	-	-	-
2008/09/08	17:50:17.35	32.333	47.383	10.18*	3.8	-	-	-	-	-
2008/09/09	21:31:26.27	32.356	47.303	9.90*	3.8	-	-	-	-	-
2008/09/18	05:20:19.69	32.331	47.375	11.40*	3.7	-	-	-	-	-
2008/09/20	05:53:02.61	32.471	47.485	-	-	-	-	-	-	-
2008/10/18	23:50:06.79	32.356	47.411	9.06*	4.0	-	-	-	-	-
2008/10/26	05:20:24.68	32.326	47.430	9.96*	3.9	-	-	-	-	-
2008/11/10	14:26:35.16	32.376	47.428	5.90*	3.5	-	-	-	-	-
2008/11/22	17:50:45.50	32.205	47.417	-	3.8	-	-	-	-	-
2008/11/26	12:44:20.59	32.197	47.428	-	-	-	-	-	-	-
2009/01/04	16:04:44.90	32.276	47.448	6.05*	3.8	-	-	-	-	-
2009/02/14	04:24:39.88	32.277	47.429	-	-	-	-	-	-	-
2009/05/30	16:06:28.45	32.280	47.503	-	-	-	-	-	-	-
2009/06/18	12:52:43.65	32.303	47.387	4.60*	3.9	-	-	-	-	-
2009/08/05	22:55:41.29	32.361	47.200	-	3.6	-	-	-	-	-
2009/08/05	23:13:30.78	32.379	47.257	-	3.7	-	-	-	-	-
2009/10/09	18:32:40.92	32.325	47.385	5.10*	4.0	-	-	-	-	-
2010/01/18	03:13:40.90	32.457	47.145	-	4.0	-	-	-	-	-
2011/12/17	23:25:34.78	32.382	47.374	-	-	-	-	-	-	-
2012/02/28	23:18:51.56	32.511	47.023	9.00	4.2	-	290	40	90	SW
				12.0	4.5	5.0	298	45	78	CMT
2012/02/28	23:41:48.55	32.416	46.902	-	-	-	-	-	-	-
2012/02/28	23:55:43.36	32.457	46.887	-	-	-	-	-	-	-
2012/02/28	23:56:54.92	32.496	46.905	-	-	-	-	-	-	-
2012/02/29	01:35:23.37	32.518	46.993	-	3.6	-	-	-	-	-
2012/02/29	02:30:11.26	32.399	46.796	-	-	-	-	-	-	-
2012/02/29	04:04:13.86	32.533	47.007	-	-	-	-	-	-	-
2012/02/29	05:10:43.19	32.530	47.052	8.62*	4.4	-	-	-	-	-
2012/02/29	05:18:49.56	32.622	47.030	-0	-	-	-	-	-	-
2012/02/29	07:09:24.14	32.340	46.994	-	-	-	-	-	-	-
2012/02/29	07:21:10.57	32.384	46.924	-0	-	-	-	-	-	-
2012/02/29	13:03:16.66	32.488	47.000	-	3.7	-	-	-	-	-
2012/03/01	02:31:05.55	32.482	47.006	-	-	-	-	-	-	-
2012/03/07	16:57:12.19	32.512	47.002	9.85*	4.2	-	-	-	-	-
2012/03/21	10:35:34.06	32.491	47.025	8.75*	3.6	-	-	-	-	-
2012/03/24	05:25:34.36	32.493	47.001	7.00	4.4	-	300	45	90	SW
				12.0	4.9	4.9	317	41	109	CMT
2012/03/25	12:28:51.01	32.460	46.975	8.95*	4.1	-	-	-	-	-
2012/04/18	18:42:58.23	32.487	47.018	7.00	4.6	-	125	45	90	SW
				12.0	5.1	5.0	129	47	95	CMT
2012/04/18	19:00:02.71	32.537	47.112	-	-	-	-	-	-	-
2012/04/18	20:04:07.44	32.581	47.148	7.00	4.1	-	120	45	90	SW
				12.0	4.4	4.9	98	55	56	CMT
2012/04/18	20:42:09.98	32.469	46.986	-	-	-	-	-	-	-
2012/04/18	20:45:57.08	32.444	47.027	-	-	-	-	-	-	-
2012/04/19	03:22:40.81	32.500	47.024	-	-	-	-	-	-	-
2012/04/19	06:27:06.32	32.512	47.128	-	-	-	-	-	-	-
2012/04/19	07:42:51.92	32.474	46.993	7.52*	4.2	-	-	-	-	-
2012/04/20	01:21:07.95	32.486	47.071	9.13*	4.7	-	310	40	95	SW
				12.0	5.1	5.2	30	37	85	CMT
2012/04/20	01:30:50.74	32.488	47.048	-	3.7	-	-	-	-	-
2012/04/20	01:40:49.75	32.381	46.879	-	-	-	-	-	-	-
2012/04/20	01:42:59.83	32.443	46.966	-	-	-	-	-	-	-

2012/04/20	01:53:32.65	32.381	46.949	-	-	-	-	-	-	-
2012/04/20	02:04:01.33	32.505	47.106	-	-	-	-	-	-	-
2012/04/20	02:49:22.42	32.509	47.031	-	-	-	-	-	-	-
2012/04/20	03:05:41.97	32.488	47.000	-	4.5	-	115	50	85	SW
				12.0	5.0	5.2	135	50	105	CMT
2012/04/20	03:07:26.59	32.539	47.011	-	4.2	-	-	-	-	-
2012/04/20	03:31:41.74	32.494	46.948	8.60*	4.0	-	-	-	-	-
2012/04/20	03:43:17.56	32.500	47.004	14.32*	3.8	-	-	-	-	-
2012/04/20	03:52:36.72	32.461	47.006	12.31*	3.8	4.8	-	-	-	-
2012/04/20	05:13:58.53	32.230	46.740	-	-	-	-	-	-	-
2012/04/20	05:22:32.51	32.570	46.998	-	3.7	-	-	-	-	-
2012/04/20	15:37:03.26	32.447	47.067	8.57	4.5	-	125	45	90	SW
				12.0	4.9	4.8	136	50	105	CMT
2012/04/20	16:17:49.99	32.467	47.074	9.55	4.3	-	300	35	95	SW
				12.0	4.7	5.0	29	34	78	CMT
2012/04/20	16:32:52.97	32.421	46.963	-	3.9	-	-	-	-	-
2012/04/20	17:19:49.27	32.514	46.967	8.63*	3.9	-	-	-	-	-
2012/04/20	21:40:48.59	32.413	47.025	-	3.6	-	-	-	-	-
2012/04/21	02:39:13.79	32.456	47.060	8.04*	4.3	-	-	-	-	-
2012/04/21	03:46:07.47	32.450	47.118	-	3.9	-	-	-	-	-
2012/04/21	05:25:08.42	32.437	47.081	7.93	4.4	-	145	45	75	SW
				18.9	5.0	5.2	156	69	114	CMT
2012/04/21	05:40:27.03	32.415	47.055	-	-	-	-	-	-	-
2012/04/21	06:13:26.82	32.414	47.111	8.00*	4.6	-	-	-	-	-
2012/04/21	06:43:15.64	32.432	47.061	-	3.5	-	-	-	-	-
2012/04/22	04:00:45.65	32.441	47.009	-	3.7	-	-	-	-	-
2012/04/22	08:13:54.46	32.415	47.078	9.70*	4.2	-	-	-	-	-
2012/04/23	16:43:00.88	32.507	47.056	-	4.2	-	-	-	-	-
2012/04/24	18:16:35.50	32.469	47.073	7.85*	4.0	-	-	-	-	-
2012/04/25	13:39:49.61	32.447	47.058	-	3.9	-	-	-	-	-
2012/04/25	14:37:50.41	32.430	47.002	-	-	-	-	-	-	-
2012/04/27	00:13:50.10	32.515	47.128	8.45*	3.7	-	-	-	-	-
2012/04/28	00:34:05.93	32.447	47.053	-	3.7	-	-	-	-	-
2012/04/29	19:03:39.47	32.511	47.116	-	3.9	-	-	-	-	-
2012/05/09	07:26:48.93	32.581	47.120	-	3.9	-	-	-	-	-
2012/05/09	08:05:46.77	32.589	47.122	-	3.7	-	-	-	-	-
2012/06/08	05:32:29.15	32.597	47.074	-	4.0	-	-	-	-	-
2012/07/25	13:08:55.91	32.527	46.988	-	3.9	-	-	-	-	-

Depths have been determined using either the surface wave amplitude spectra method or teleseismic body wave observations (* depth fixed using teleseismic body wave data). Source mechanisms estimated using the observed surface wave amplitude spectra (SW) and the published centroid moment tensor (CMT) solutions (http://www.globalcmt.org, GCMT) are also listed. The values for m_b are those published in the REB, unless CMT is stated in the method column, when the values for m_b are those published by the GCMT. The values for m_w are those published by the GCMT.

844

Figure 1

Figure 2

Figure 3

Figure 4

Figure 5

Figure 6

Figure 7

Figure 1

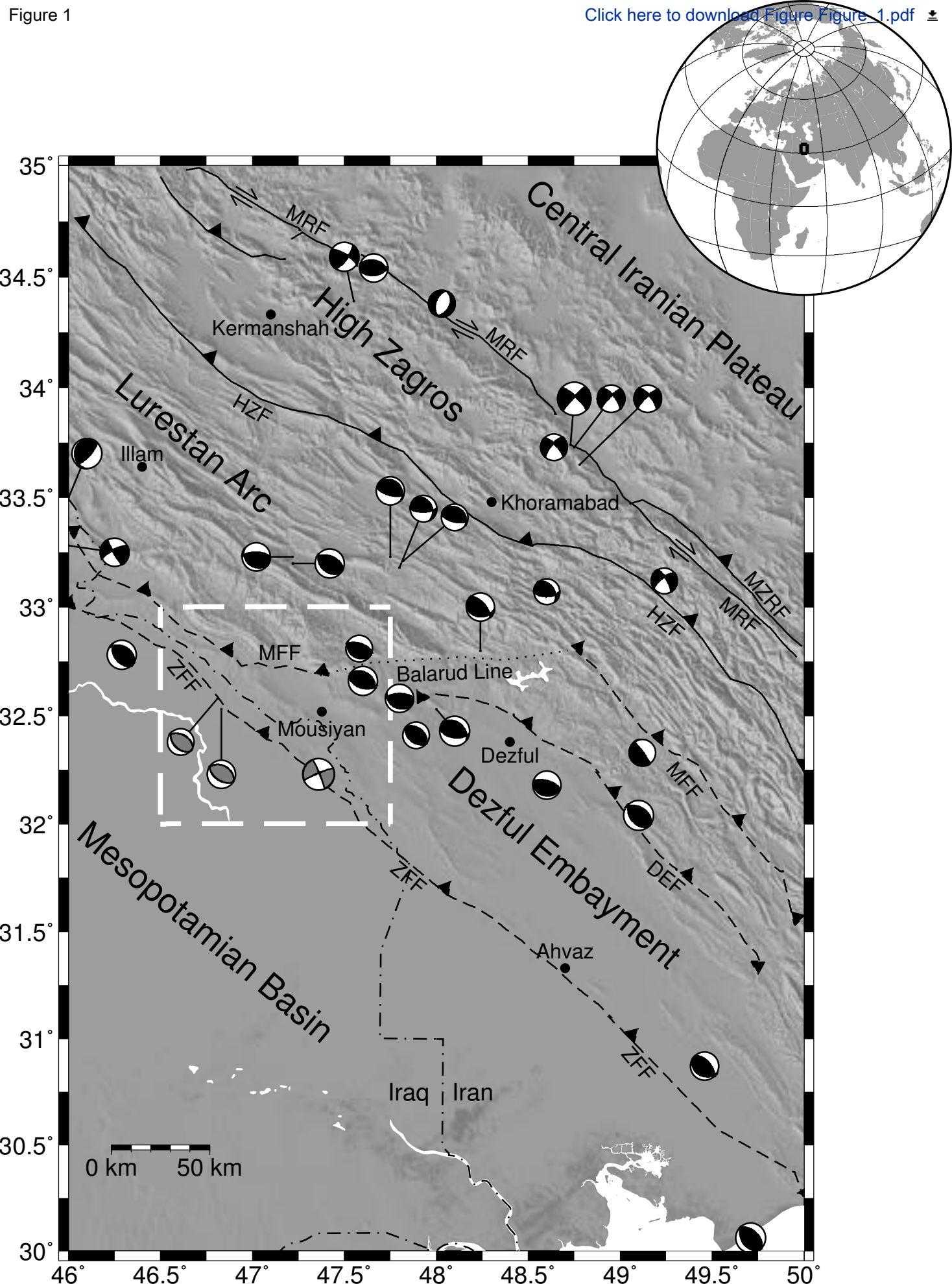

Figure 2

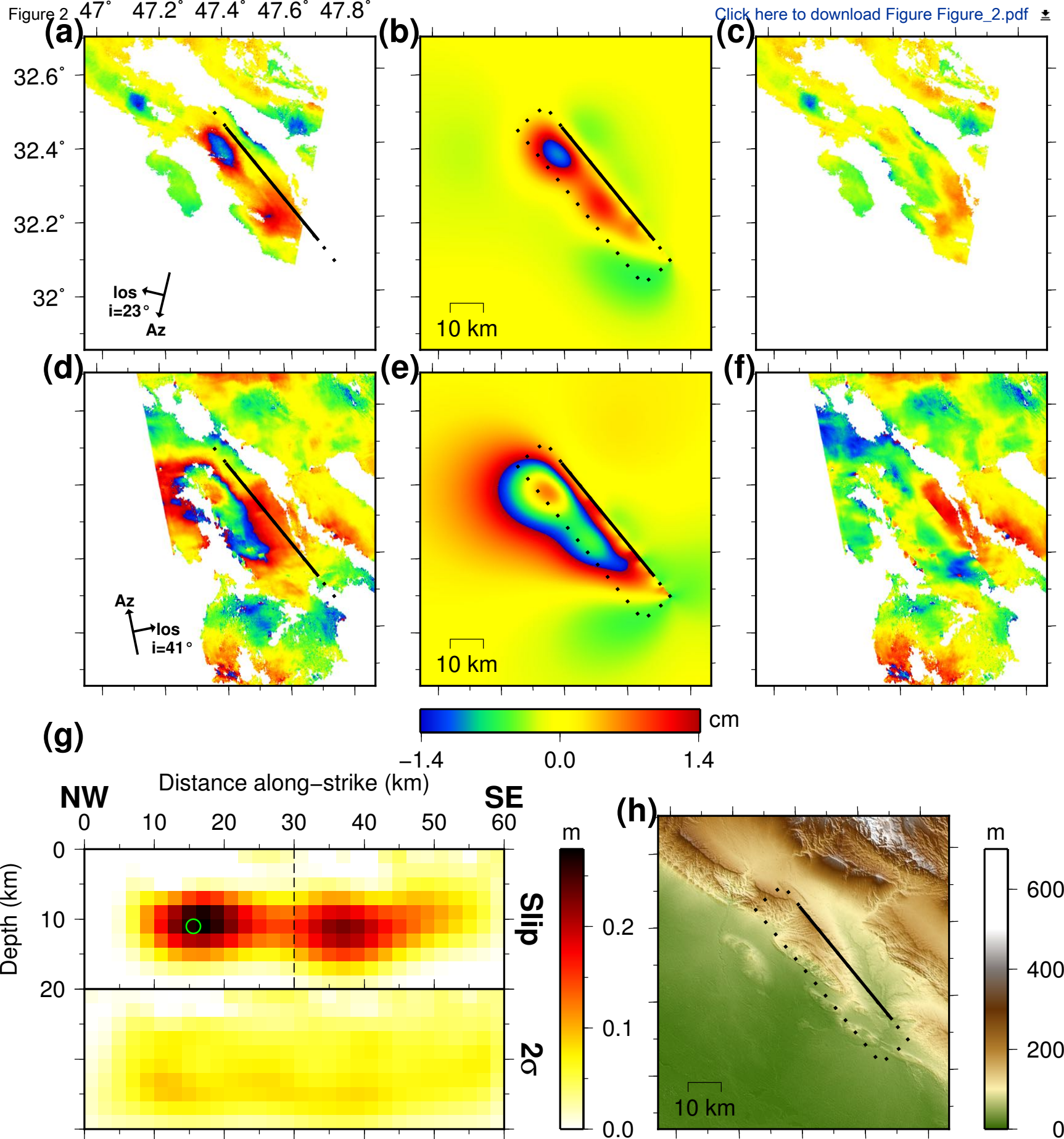

Figure 3

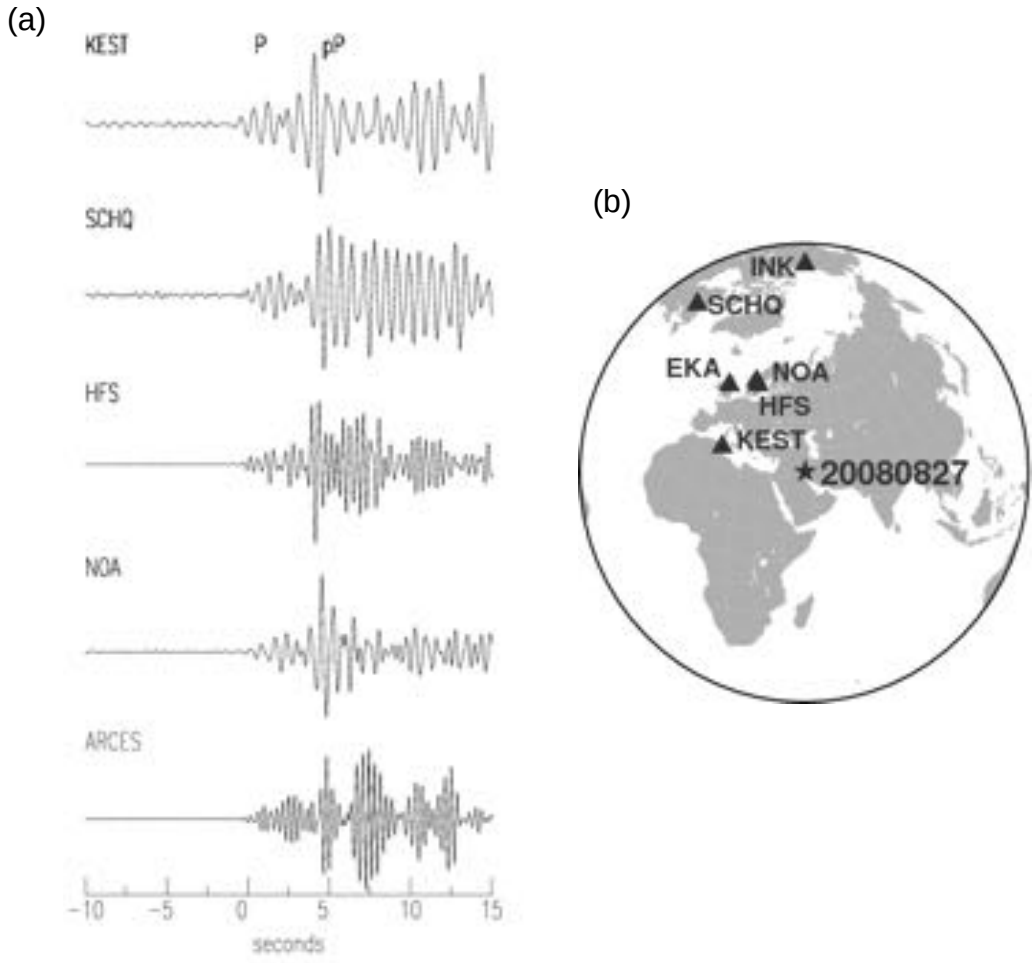

Figure 4

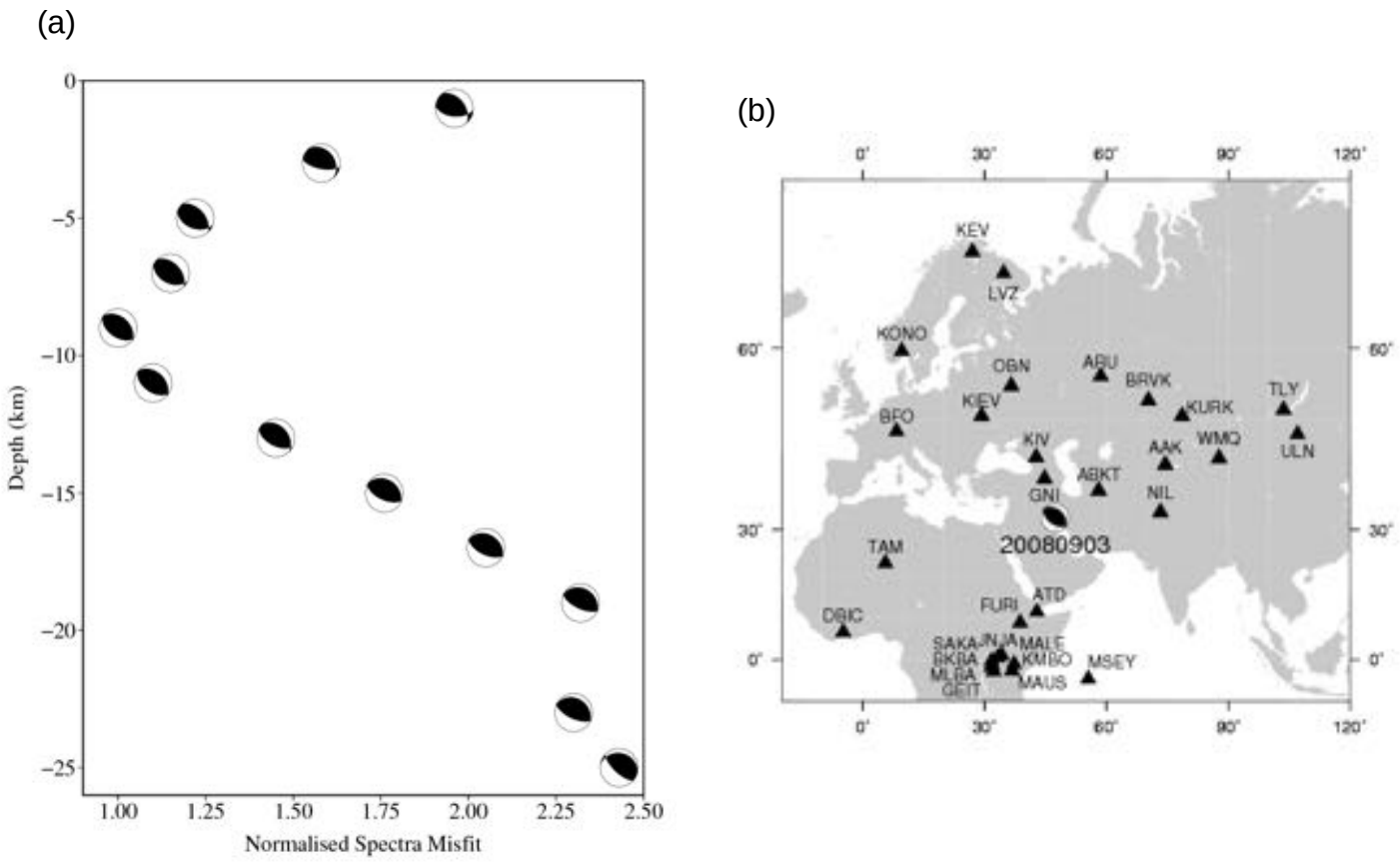

Figure 5

Click here to download Figure Figure_5.pdf

(a)

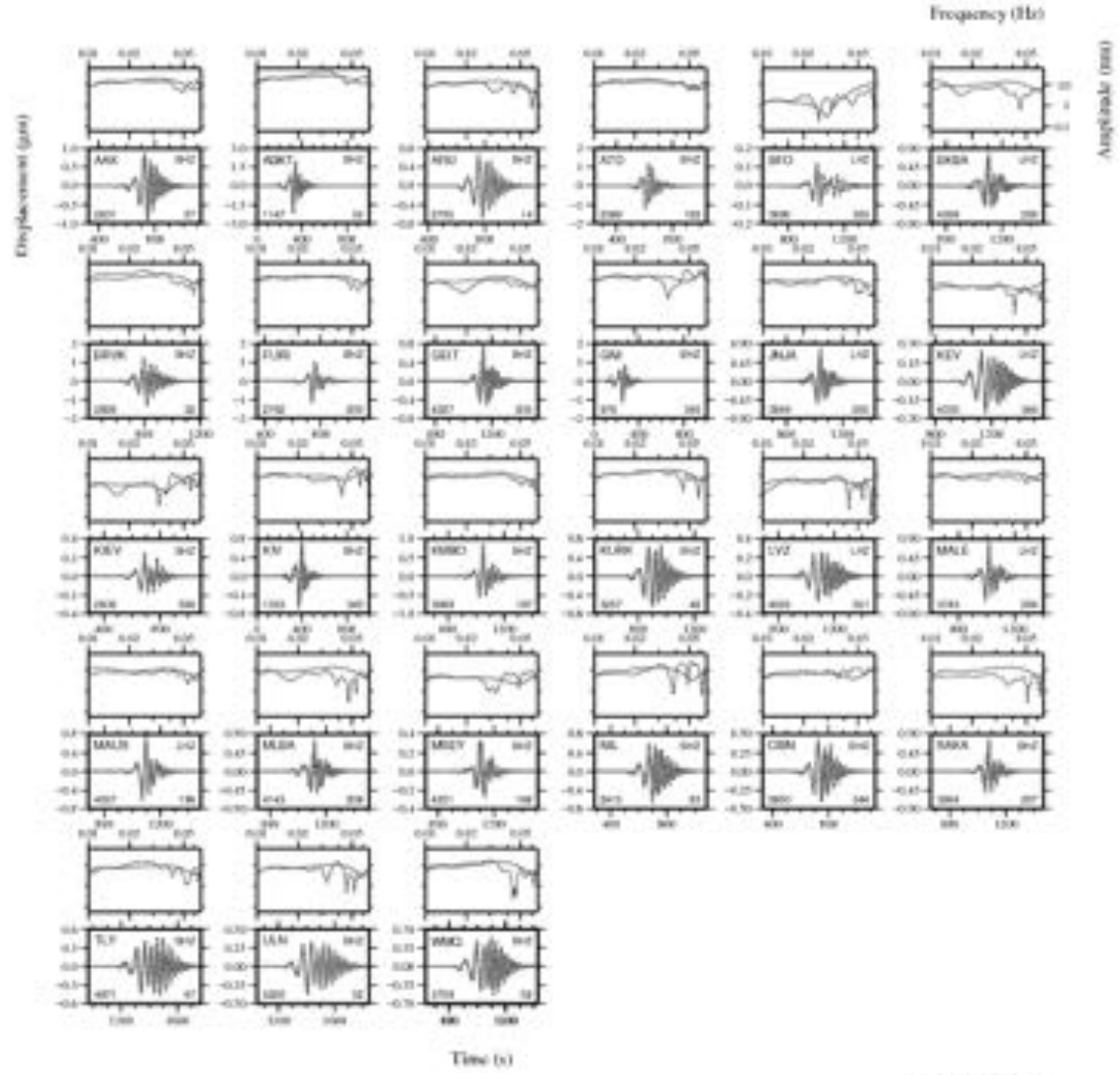

(b)

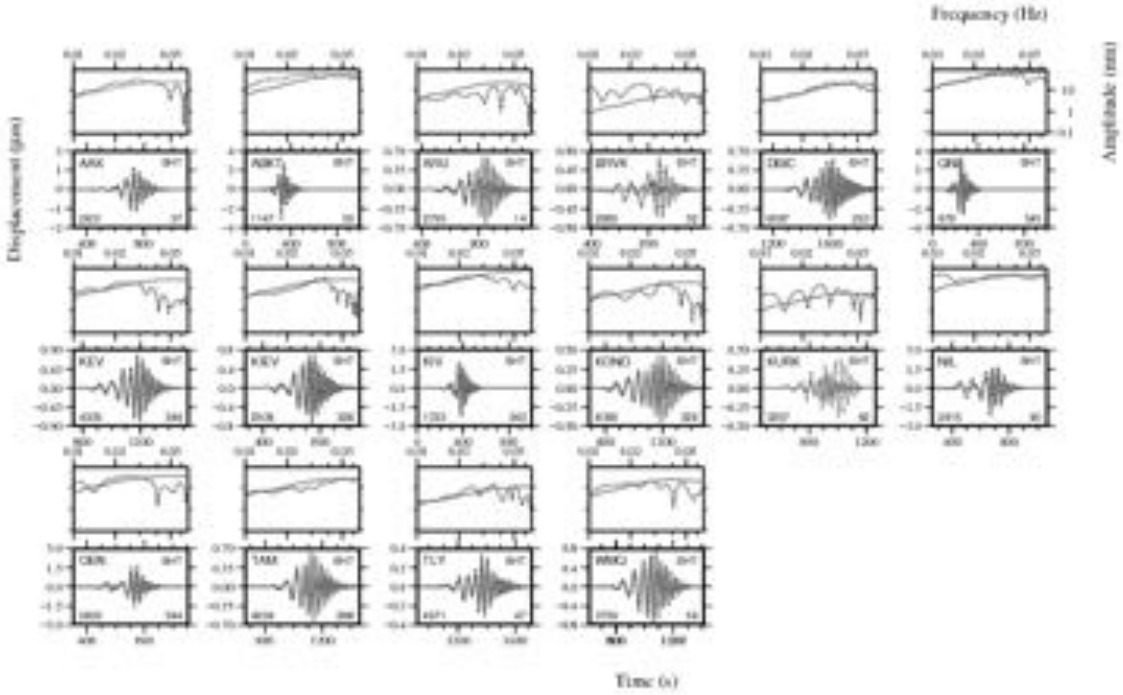

Figure 6

Click here to download Figure Figure_6.pdf

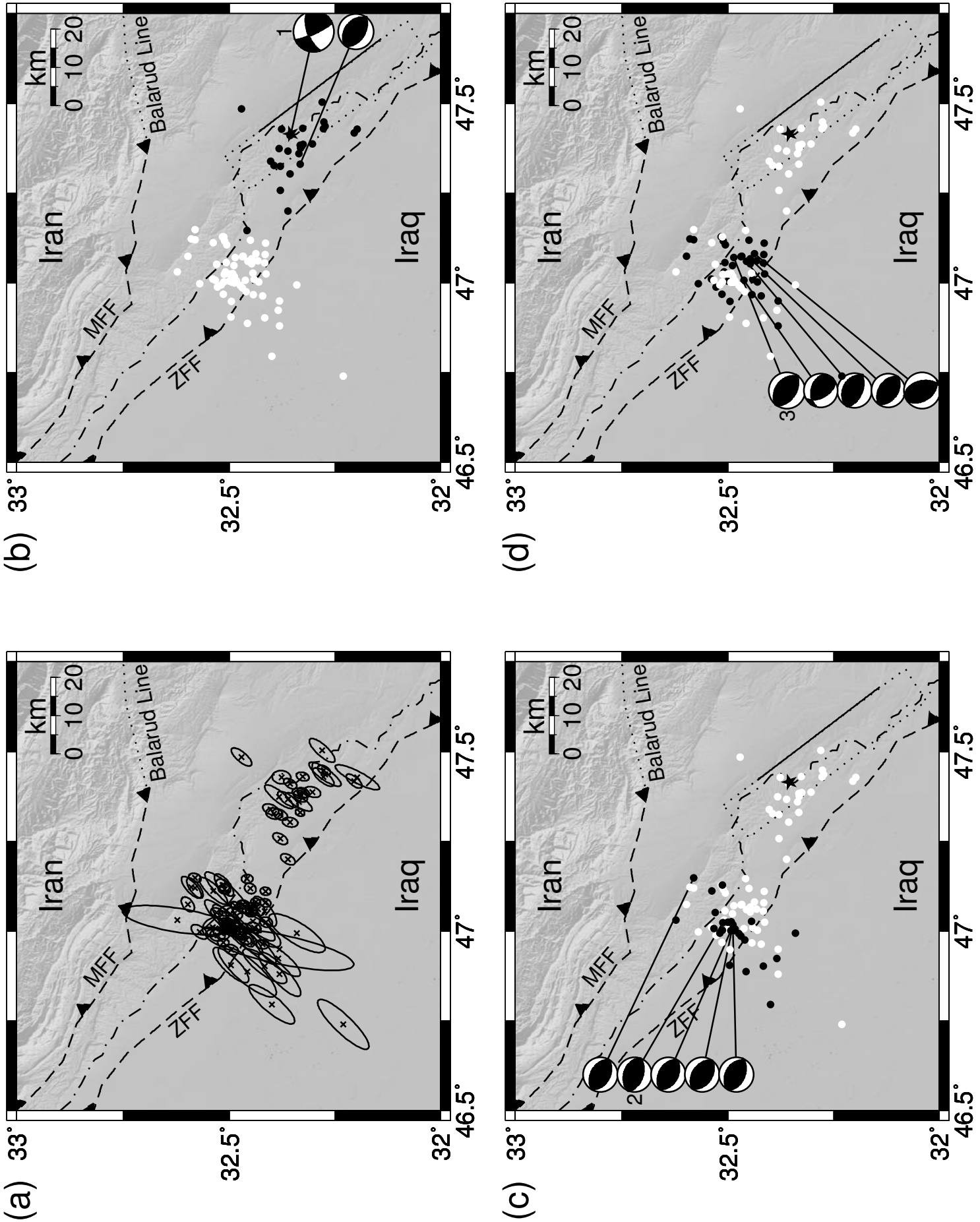

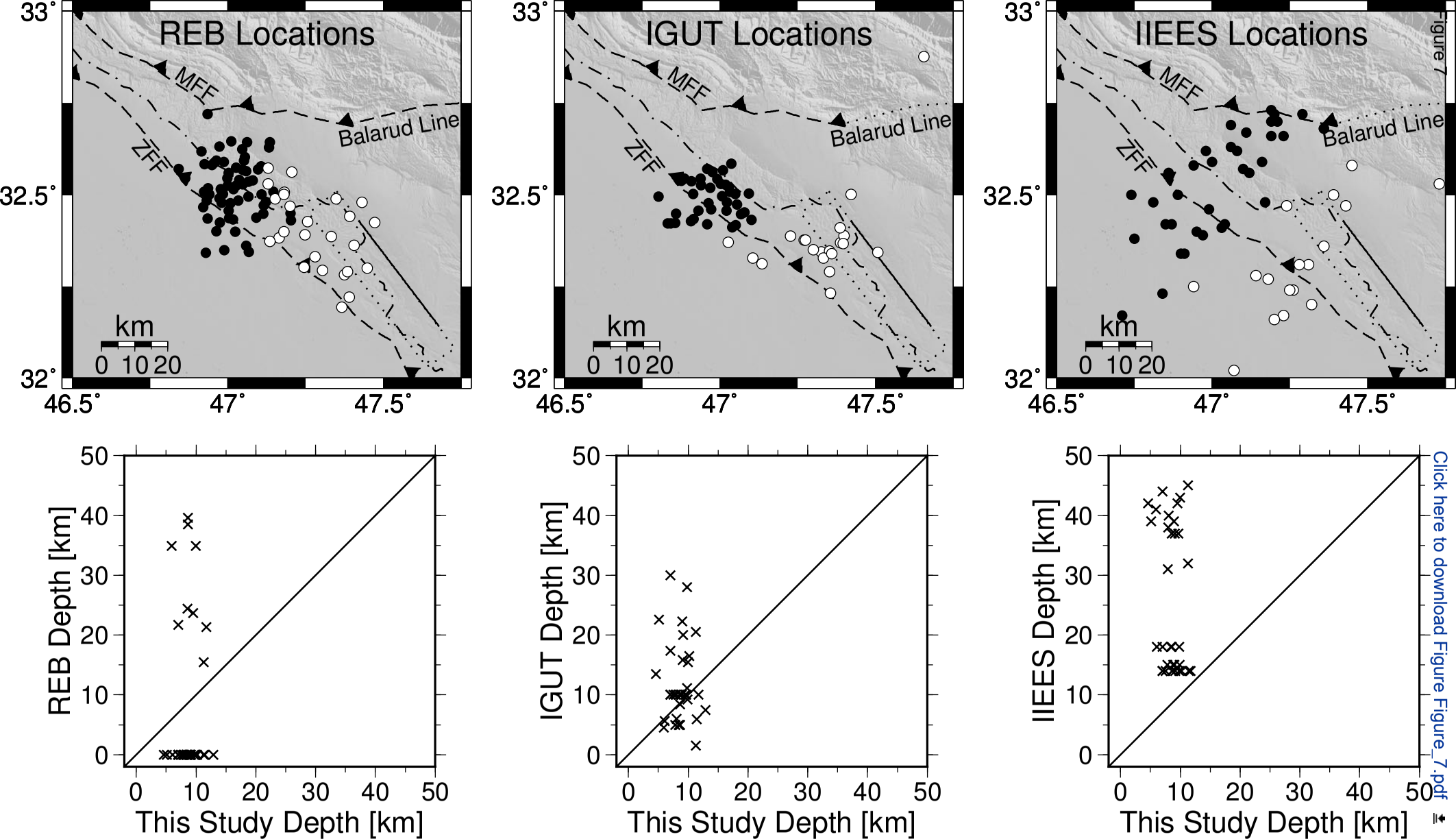
REB Locations
IGUT Locations
IIEES Locations
MFF
ZFF
Balarud Line
km
0 10 20
33˚
32.5˚
32˚
46.5˚
47˚
47.5˚
REB Depth [km]
IGUT Depth [km]
IIEES Depth [km]
This Study Depth [km]
0
10
20
30
40
50
Figure 7
Click here to download Figure Figure_7.pdf

Figure S1

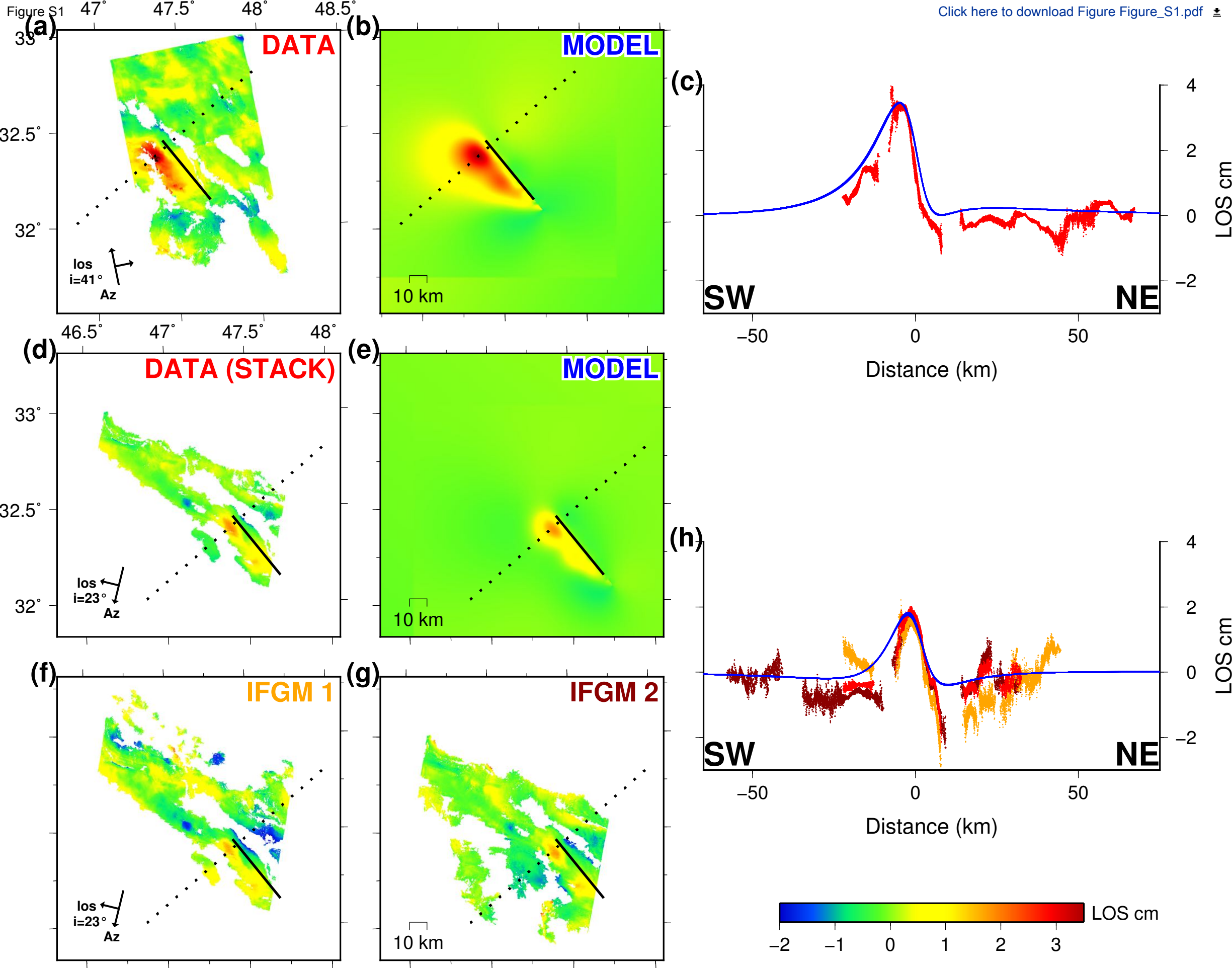

Figure S3

Click here to download Figure Figure_S3.pdf

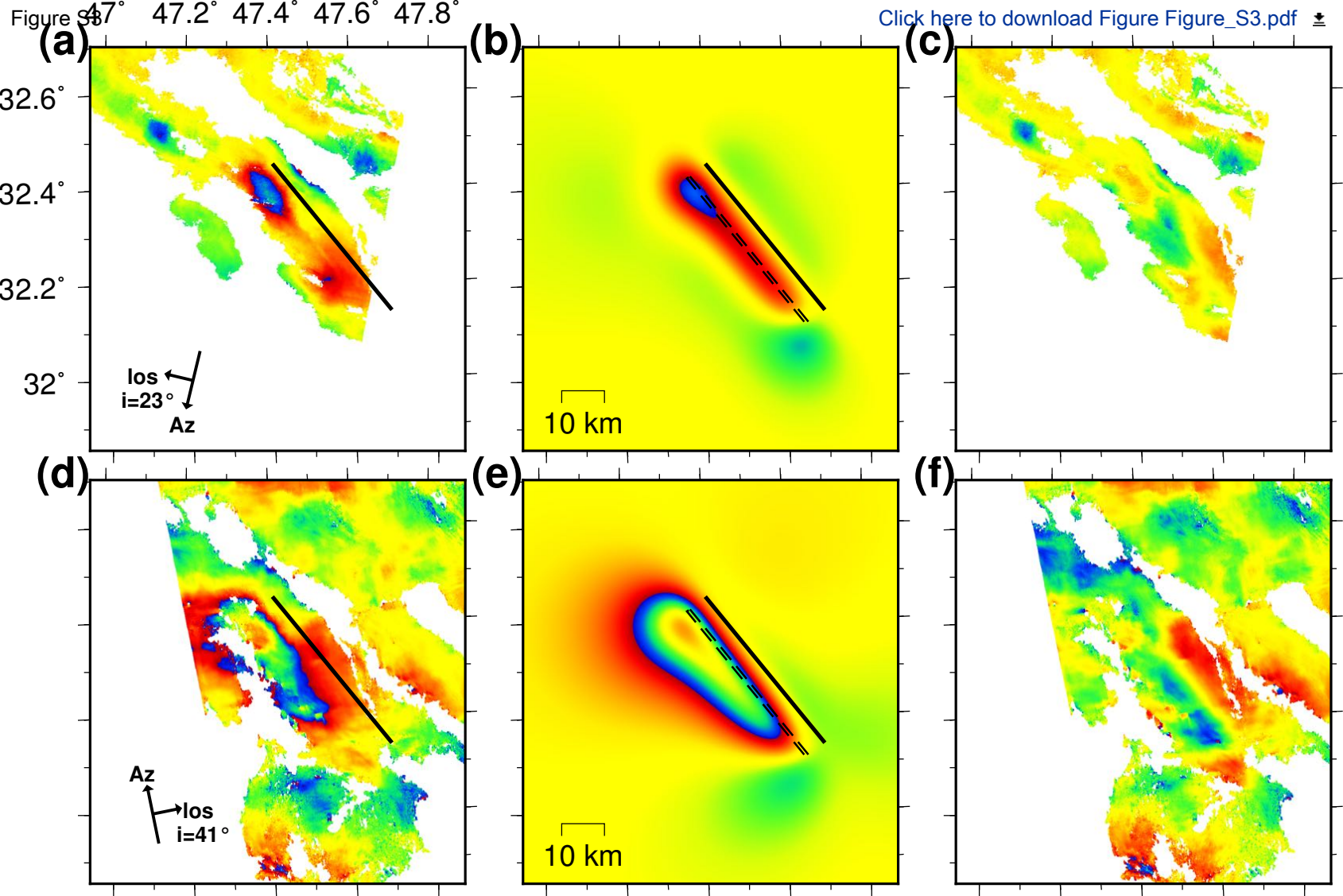

Figure S2.

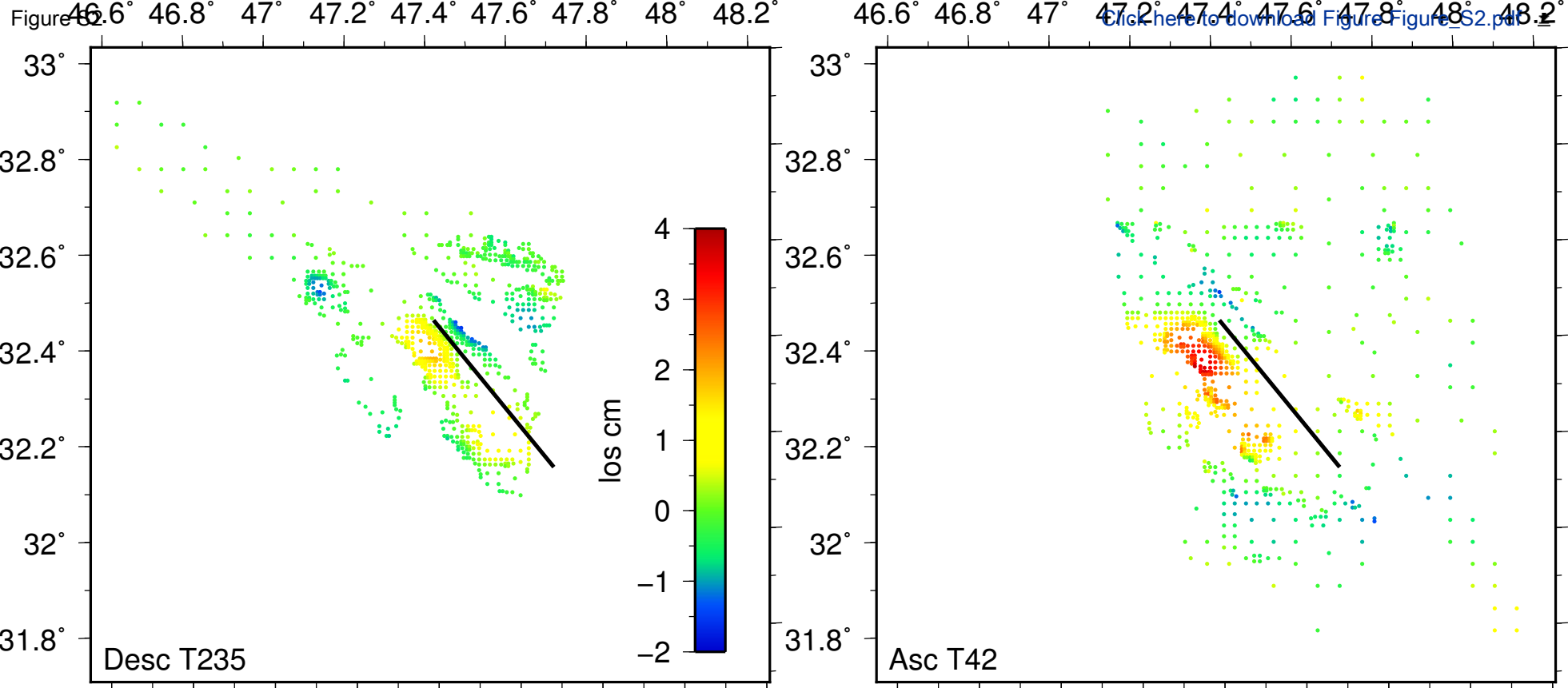

Figure S4

Click here to download Figure Figure_S4.pdf

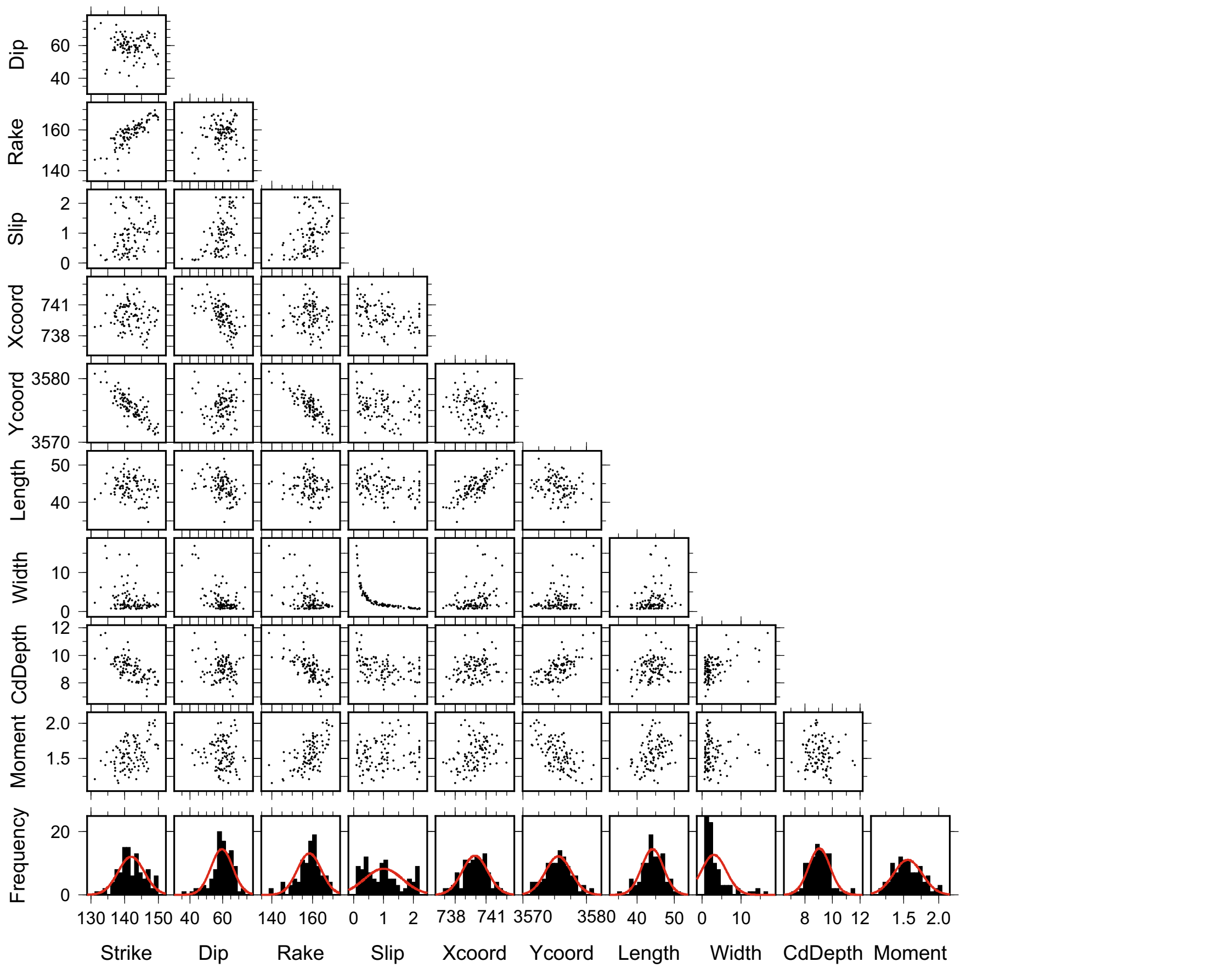

Figure S5

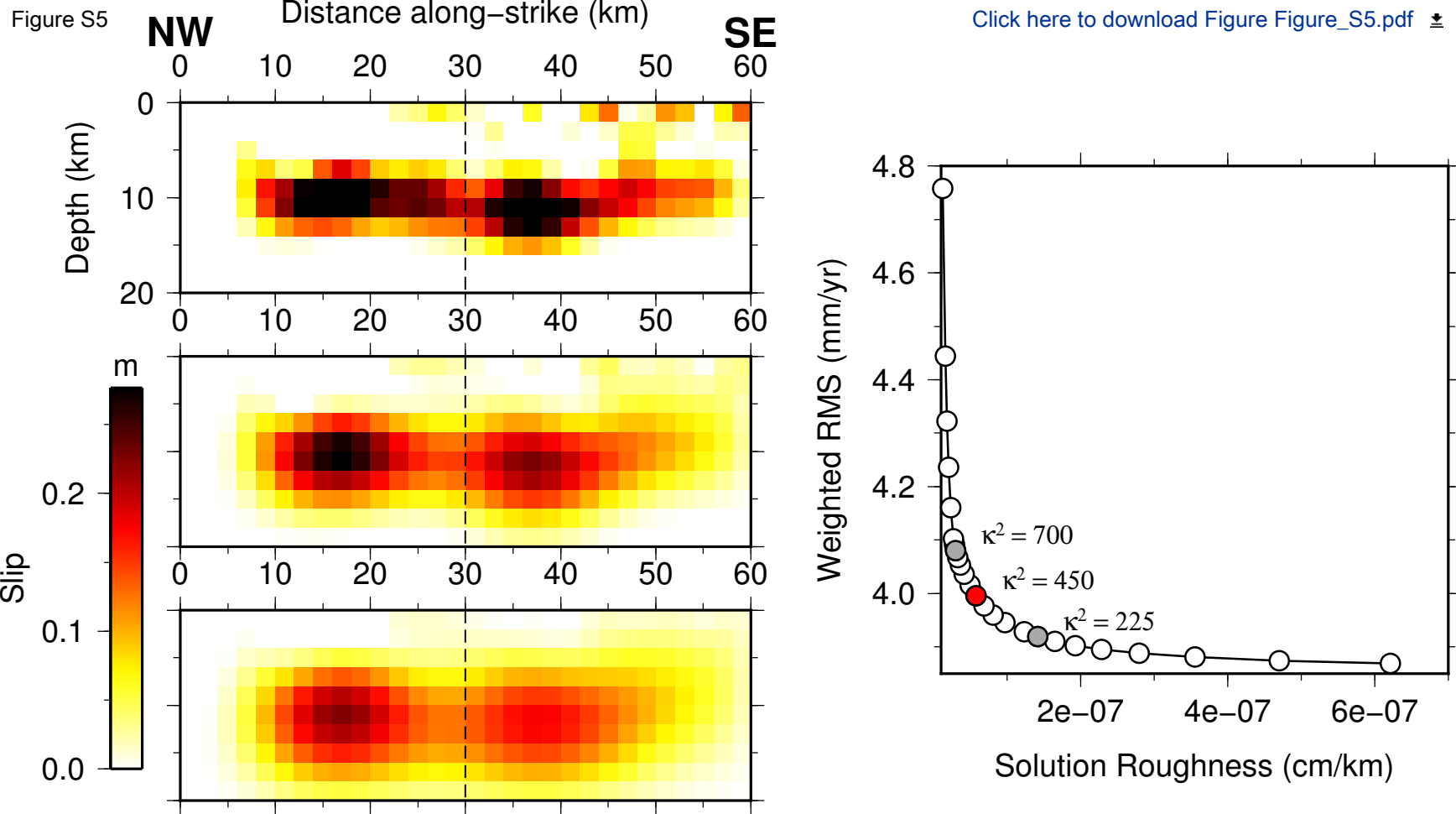

Figure S6

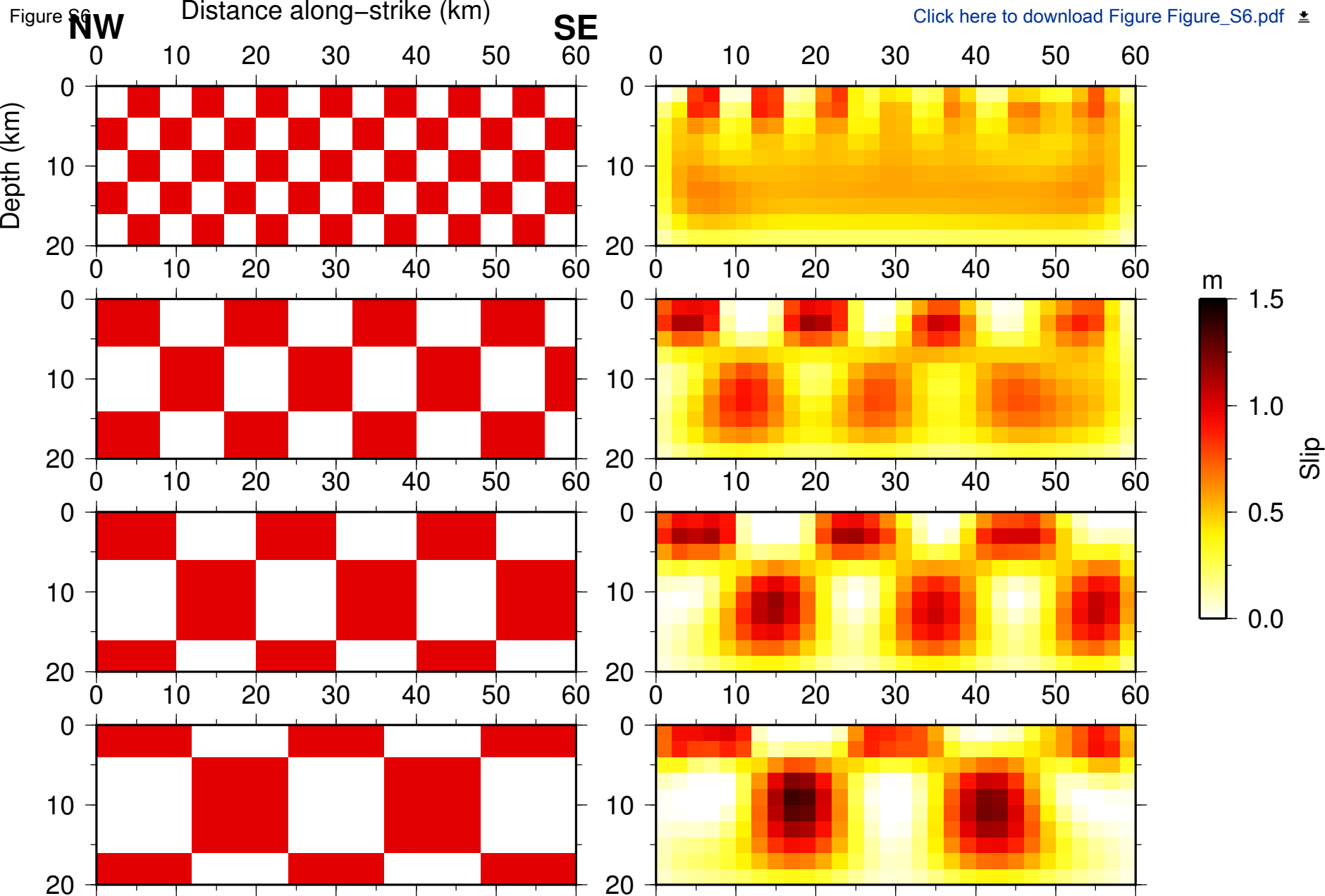

Click here to download Figure Figure_S6.pdf

The 2008 and 2012 Moosiyan Earthquake Sequences: rare insights into the role of strike slip and thrust faulting within the Simply Folded Belt (Iran).

Stuart E.J. Nippress, Ross Heyburn, and R.J. Walters

The supplementary information includes additional figures regarding the InSAR modeling and resolution of the InSAR slip models for the 27th August 2008 earthquake.

Figure S1. InSAR data and predicted displacements from distributed slip inversion for the 27th August 2008 earthquake. (a) A single ascending track ENVISAT interferogram spanning the interval 25th of January 2007 to 9th of April 2009. Solid black line shows the up-dip projection of the fault plane, and dashed line shows the location of profile (c). Black arrows show the flight direction of ENVISAT (Az), the line-of-sight direction (los) and the incidence angle at the center of the interferogram (i). (b) Predicted displacements from the distributed slip inversion (Figure 2), projected into the same line-of-sight geometry as in (a). (c) Profile to the right shows LOS displacement along the dashed profile line for both the data (red) and the model prediction (blue). (d) and (e) are the same as (a) and (b) but for a stack of two descending track ENVISAT SAR interferograms spanning the intervals 23rd of February 2006 to 22nd of July 2010 and 15th of November 2007 to 4th of March 2010. The individual interferograms are shown in (f) and (g), and profile (h) shows the displacements from these two interferograms (orange and dark red), along with those from the stack (red) and those predicted by the model (blue).

Figure S2. The distribution of subsampled datapoints used to model the 27th August 2008 earthquake, for the stacked descending dataset (left) and the ascending interferogram (right). The colour of the points shows displacement in the line-of-sight of the satellite, and the black solid line shows the location of the model fault.

Figure S3. InSAR data and elastic dislocation model for the 27th August 2008 earthquake. (a) Stack of two descending track ENVISAT SAR interferograms spanning the intervals 23rd of February 2006 to 22nd of July 2010 and 15th of November 2007 to 4th of March 2010. Black arrows show the flight direction of ENVISAT (Az), the line-ofsight direction (los) and the incidence angle at the center of the interferogram (i). (b) Best-fitting elastic dislocation model for uniform slip on a rectangular plane (Table 1), obtained from the joint inversion of both ascending and descending track InSAR data. The solid black line shows the surface trace of the uniform slip solution (Table 1). (c) Residuals between the data and the model. (d), (e) and (f) are the same as (a), (b) and (c) but for a single ascending track ENVISAT interferogram spanning the interval 25th of January 2007 to 9th of April 2009.

Figure S4. Fault parameter uncertainties and trade-offs for the uniform slip InSAR model of the 27th August 2008 Mw 5.8 earthquake. Uncertainties and trade-offs are calculated using a Monte Carlo approach, from the inversion of one hundred datasets perturbed with realistic noise. Histograms show uncertainties for individual model

parameters and scatterplots show trade-offs between parameters. The red lines overlain on histograms are the Gaussian distributions fitted to the data. Strike, dip and rake are in degrees, slip is in m, Xcoord and Ycoord are X and Y coordinates of the centre of the surface projection of the fault plane in UTM km (zone 38N), length, width and centroid depth (CdDepth) of the fault plane are in km, and moment is in units of 10^{18} Nm.

Figure S5. Influence of the choice of Laplacian smoothing parameter (kappa2) on slip distributions for the 27th August 2008 earthquake. (left) Slip distributions are shown as in Figure 2 for three choices of smoothing parameter, producing our preferred model (centre), a rougher solution (top) and a smoother solution (bottom). The choice of smoothing parameter represents a trade-off between reducing RMS misfit and solution roughness (right). Our chosen solution is shown as a red circle, and the two gray circles represent the pictured rougher and smoother solutions. Note that all three solutions feature double maxima in slip.

Figure S6. Resolution test for slip distributions for the 27th August 2008 earthquake, showing checkerboard inputs (left) and recovered slip (right) for square patches of size (from top to bottom) 4 km, 8 km, 10 km and 12 km. The strength of Laplacian used when inverting these synthetic data is the same as for our chosen solution.